

# Jost-matrix analysis of the resonance ${}^5\text{He}^*(\frac{3}{2}^+)$ near the $dt$ -threshold

S.A. Rakityansky<sup>a\*</sup> and S.N. Ershov<sup>b†</sup>

<sup>a</sup>Department of Physics, University of Pretoria, Pretoria, South Africa

<sup>b</sup>Joint Institute for Nuclear Research, Dubna, Russia

March 24, 2022

## Abstract

Experimental data on the  $n\alpha$  and  $dt$  collisions in the quantum state  $J^\pi = \frac{3}{2}^+$  near the  $dt$ -threshold are fitted using the semi-analytic multi-channel Jost matrix with proper analytic structure and some adjustable parameters. Then the spectral points are sought as zeros of the Jost matrix determinant (which correspond to the  $S$ -matrix poles) at complex energies. The correct analytic structure makes it possible to calculate the fitted Jost matrix on any sheet of the Riemann surface whose topology involves not only the square-root but also the logarithmic branching caused by the Coulomb interaction. Within a distance of 100 keV above the  $dt$ -threshold, three  $\frac{3}{2}^+$ -resonances are found on the non-physical sheet of the Riemann surface. Several  $S$ -matrix (shadow) poles on the other sheets of this surface are located as well.

## 1 Introduction

The five-nucleon system  ${}^5\text{He}$  is unstable even in its “ground state”, which actually is a resonance lying 798 keV above the  $n\alpha$ -threshold [1]. The other decay channel,  $dt$ , opens up much higher, at 16.792 MeV above the ground state [1].

This system plays an important role in nuclear astrophysics as well as in the man-made thermonuclear fusion (for both the peaceful and military purposes). This is why so many

---

\*e-mail: rakitsa@up.ac.za

†e-mail: ershov@theor.jinr.ru

publications have been devoted to experimental and theoretical studies of its properties (see, for example, few selected papers [2–18]). One of the controversial issues in these studies, that still remains vague, is the nature of the resonant state with  $J^\pi = \frac{3}{2}^+$  lying at around  $\sim 50$  keV above the  $dt$ -threshold. The majority of theoretical analyses claim that this state is a superposition of a conventional resonance and a so-called “shadow”  $S$ -matrix pole that supposedly is located somewhere on one of the non-physical sheets of the energy Riemann-surface and somehow affects from there the physical collisions.

The main task of our present paper is to clarify the nature of that  ${}^5\text{He}^*(\frac{3}{2}^+)$ -resonance. As the experimental data, we use the partial cross sections for the four coupled channels,  $n\alpha(\ell = 2, s = 1/2)$ ,  $dt(\ell = 0, s = 3/2)$ ,  $dt(\ell = 2, s = 1/2)$ , and  $dt(\ell = 2, s = 3/2)$ , that we obtain using the  $R$ -matrix parametrization given in Ref. [5]. A closer look at the inter-channel cross sections leads us to the conclusion that only the first two of them, namely,  $n\alpha(\ell = 2, s = 1/2)$  and  $dt(\ell = 0, s = 3/2)$ , are strongly coupled to each other. It is therefore reasonable to describe the  $\frac{3}{2}^+$ -resonances near the  $dt$ -threshold within the corresponding two-channel model. This is what we do in the present paper.

The novelty of our analysis consists in using the multi-channel Jost matrix for fitting the partial cross sections. These cross sections are extracted from the available  $R$ -matrix parametrization of a large collection of experimental data. Therefore, in this way, we indirectly fit the data. After the fitting at real energies, the Jost matrix is considered at complex  $E$ , where the zeros of its determinant correspond to the poles of the  $S$ -matrix.

We use a special representation of the multi-channel Jost matrix suggested in Refs. [19, 20], where the Jost matrix is given as a sum of two terms and each term is factorized in a product of two matrices. One of these matrices is an unknown analytic single-valued function of the energy and the other is given explicitly as a function of the channel momenta and is responsible for the branching of the Riemann surface. The unknown single-valued matrices are parametrized and the parameters are found via fitting the available experimental data.

When using the semi-analytic representation of the Jost matrix, where the factors responsible for the topology of the Riemann surface are given explicitly, it is easy to explore the behaviour of the Jost matrix on all the sheets of the Riemann surface. In this way we are able to accurately locate the resonance poles and to examine the existence of the “shadow” poles.

## 2 Jost matrices

In this Section, we give a definition of the Jost matrices, show how they are related to the observable quantities, and discuss their analytic properties. All the details omitted here, can be found in Refs. [19–21].

${}^5\text{He}^*(\frac{3}{2}^+)$	$\gamma$	$n\alpha$	$dt$		
	$(\ell, s)$	$(2, \frac{1}{2})$	$(0, \frac{3}{2})$	$(2, \frac{1}{2})$	$(2, \frac{3}{2})$
	$n$	1	2	3	4
barriers		centrifugal	Coulomb	centrifugal + Coulomb	centrifugal + Coulomb
relative kinetic energies		$\sim 18 \text{ MeV}$	$\sim 50 \text{ keV}$	$\sim 50 \text{ keV}$	$\sim 50 \text{ keV}$

Table 1: Four possible combinations of the set  $(\gamma, \ell, s)$  for the  $\frac{3}{2}^+$  state of  ${}^5\text{He}$  just above the  $dt$ -threshold; types of the potential barriers in each of the channels; and the relative kinetic energies of the fragments in the resonance state.

## 2.1 Definition

We restrict our consideration to the binary multi-channel reactions. In such a reaction the colliding particles may either change their internal states ( $a + b \rightarrow a^* + b^*$ ) or transform themselves into another pair of particles ( $a + b \rightarrow c + d$ ). Generally speaking, the masses of the particles (and therefore the total energy) in the initial and final state are different and thus the channels  $ab$ ,  $a^*b^*$ ,  $cd$ , etc. have different thresholds. Each of these different two-particle states is labeled by the symbol  $\gamma$ . For a given  $\gamma$ , the particles may have several possible combinations of the orbital angular momentum,  $\ell$  and the total spin  $s$ . Each combination of them (despite the fact that the threshold energy is the same) is treated as a separate channel. The total angular momentum  $J$  and the parity  $\pi$  are the same for all the channels and, in order to simplify the notation, we omit them. Therefore a channel is specified by the three quantum numbers,  $(\gamma, \ell, s)$ . Each possible combination of the numbers  $(\gamma, \ell, s)$  can be assigned a single sequential number  $n = 1, 2, \dots, N$ , where  $N$  is the total number of the channels taken into account in a particular model. For example, in the problem we consider in the present paper, namely, the quasi-bound state of  ${}^5\text{He}$  with  $J^\pi = \frac{3}{2}^+$  near the  $dt$ -threshold, there are four channels listed in Table 1.

The system of the  $N$ -channel radial Schrödinger equations,

$$\left[ \partial_r^2 + k_n^2 - \frac{\ell_n(\ell_n + 1)}{r^2} - \frac{2k_n\eta_n}{r} \right] u_n(E, r) = \sum_{n'=1}^N V_{nn'}(r) u_{n'}(E, r) \quad , \quad (1)$$

$$n = 1, 2, \dots, N \quad ,$$

where  $k_n$ ,  $\ell_n$ ,  $\eta_n$ , and  $V$  are the channel momentum, channel angular momentum, channel

Sommerfeld parameter, and the short-range part of the potential, has  $2N$  linearly independent column solutions,  $(u_1, u_2, \dots, u_N)^T$ . Since this differential equation has a regular singular point at  $r = 0$ , only half of these solutions are regular at  $r = 0$  (see, for example, Ref. [22]). These  $N$  regular columns form a regular basis, i.e. any other regular solution (the physical solution in particular) is their linear combination. Putting these regular columns together, we obtain a square  $(N \times N)$ -matrix  $\phi(E, r)$ . At large distances the right-hand side of Eq. (1) vanishes and it becomes pure Coulomb equation. This means that, when  $r \rightarrow \infty$ , each column of matrix  $\phi(E, r)$  becomes a linear combination of the pure Coulomb functions. For the case of  $N = 2$  this can be written as

$$\begin{aligned} \phi(E, r) \xrightarrow{r \rightarrow \infty} & \begin{bmatrix} H_{\ell_1}^{(-)}(\eta_1, k_1 r) e^{i\sigma_{\ell_1}} & 0 \\ 0 & H_{\ell_2}^{(-)}(\eta_2, k_2 r) e^{i\sigma_{\ell_2}} \end{bmatrix} \begin{bmatrix} f_{11}^{(\text{in})}(E) & f_{12}^{(\text{in})}(E) \\ f_{21}^{(\text{in})}(E) & f_{22}^{(\text{in})}(E) \end{bmatrix} + \\ & + \begin{bmatrix} H_{\ell_1}^{(+)}(\eta_1, k_1 r) e^{-i\sigma_{\ell_1}} & 0 \\ 0 & H_{\ell_2}^{(+)}(\eta_2, k_2 r) e^{-i\sigma_{\ell_2}} \end{bmatrix} \begin{bmatrix} f_{11}^{(\text{out})}(E) & f_{12}^{(\text{in})}(E) \\ f_{21}^{(\text{out})}(E) & f_{22}^{(\text{in})}(E) \end{bmatrix}, \quad (2) \end{aligned}$$

where

$$H_{\ell}^{(\pm)}(\eta, kr) = F_{\ell}(\eta, kr) \mp iG_{\ell}(\eta, kr) \xrightarrow{r \rightarrow \infty} \mp i \exp \left\{ \pm i \left[ kr - \eta \ln(2kr) - \frac{\ell\pi}{2} + \sigma_{\ell} \right] \right\} \quad (3)$$

are the in-coming and out-going Coulomb spherical waves,  $\sigma_{\ell}(E)$  is the pure Coulomb phase shift, and the combination coefficients are organized in the  $(N \times N)$ -matrices  $\mathbf{f}^{(\text{in/out})}(E)$  that are called the Jost matrices. In a sense, they are the amplitudes of the incoming and outgoing waves in the asymptotic behaviour of the regular solution. Of course the matrices  $\mathbf{f}^{(\text{in})}$  and  $\mathbf{f}^{(\text{out})}$  are not completely independent. At real collision energies they are complex conjugate of each other. When  $E$  is complex, the relation between them becomes more complicated. Their values on different sheets of the Riemann surface are related as is shown in the Appendix A.

## 2.2 Observables

Since the columns of matrix  $\phi(E, r)$  constitute a regular basis, a physical wave function, i.e. a column  $\mathbf{u}(E, r)$ , is their linear combination (for the sake of clarity, we write the formulae

for  $N = 2$ ):

$$\begin{aligned} \mathbf{u}(E, r) &= \begin{bmatrix} u_1(E, r) \\ u_2(E, r) \end{bmatrix} = \begin{bmatrix} \phi_{11}(E, r) \\ \phi_{21}(E, r) \end{bmatrix} c_1 + \begin{bmatrix} \phi_{12}(E, r) \\ \phi_{22}(E, r) \end{bmatrix} c_2 \\ &= \begin{bmatrix} \phi_{11}(E, r) & \phi_{12}(E, r) \\ \phi_{21}(E, r) & \phi_{22}(E, r) \end{bmatrix} \begin{pmatrix} c_1 \\ c_2 \end{pmatrix} = \boldsymbol{\phi}(E, r) \mathbf{c} . \end{aligned} \quad (4)$$

The combination coefficients  $c_n$  are to be chosen to satisfy certain physical boundary conditions at infinity. For a spectral point (either bound or a resonant state) the physical wave function should only have the outgoing waves in its asymptotic behaviour,

$$\begin{aligned} \mathbf{u}(E, r) &\xrightarrow{r \rightarrow \infty} \begin{bmatrix} H_{\ell_1}^{(-)}(\eta_1, k_1 r) e^{i\sigma_{\ell_1}} & 0 \\ 0 & H_{\ell_2}^{(-)}(\eta_2, k_2 r) e^{i\sigma_{\ell_2}} \end{bmatrix} \mathbf{f}^{(\text{in})}(E) \mathbf{c} + \\ &+ \begin{bmatrix} H_{\ell_1}^{(+)}(\eta_1, k_1 r) e^{-i\sigma_{\ell_1}} & 0 \\ 0 & H_{\ell_2}^{(+)}(\eta_2, k_2 r) e^{-i\sigma_{\ell_2}} \end{bmatrix} \mathbf{f}^{(\text{out})}(E) \mathbf{c} . \end{aligned} \quad (5)$$

This can only be achieved if

$$\mathbf{f}^{(\text{in})}(E) \mathbf{c} = \begin{bmatrix} f_{11}^{(\text{in})}(E) & f_{12}^{(\text{in})}(E) \\ f_{21}^{(\text{in})}(E) & f_{22}^{(\text{in})}(E) \end{bmatrix} \begin{pmatrix} c_1 \\ c_2 \end{pmatrix} = 0 , \quad (6)$$

which is a homogeneous system of linear equations for the unknown combination coefficients  $c_n$ . It has a non-zero solution if and only if

$$\det \begin{bmatrix} f_{11}^{(\text{in})}(E) & f_{12}^{(\text{in})}(E) \\ f_{21}^{(\text{in})}(E) & f_{22}^{(\text{in})}(E) \end{bmatrix} = 0 . \quad (7)$$

The roots  $E = \mathcal{E}_n$  of this equation at real negative energies ( $\mathcal{E}_n < 0$ ) correspond to the bound states, and the roots at complex energies ( $\mathcal{E}_n = E_r - i\Gamma/2$ ) give us the resonances.

In a similar way it can be easily shown (see, for example, Refs. [19, 21]) that the scattering is determined by the “ratio” of the amplitudes of the out-going and in-coming waves, i.e. by the  $S$ -matrix,

$$\mathbf{S}(E) = \mathbf{f}^{(\text{out})}(E) [\mathbf{f}^{(\text{in})}(E)]^{-1} . \quad (8)$$

It is obvious that the roots of eq. (7) correspond to the poles of the  $S$ -matrix. It can be shown (see, for example, Ref. [23]) that the reaction cross section is determined by the reaction amplitude,

$$f_{n' \leftarrow n}^J = \frac{S_{n'n}^J - \delta_{n'n}}{2ik_n} i^{\ell_n - \ell_{n'}} , \quad (9)$$

that is expressed via the corresponding  $S$ -matrix. The partial cross section (describing the transition between any two particular channels) can be obtained as

$$\sigma^J(\gamma' \ell' s' \leftarrow \gamma \ell s) = 4\pi \frac{\mu_\gamma k_{\gamma'}}{\mu_{\gamma'} k_\gamma} \cdot \frac{2J+1}{2s+1} |f_{n'n}^J|^2 , \quad (10)$$

where  $\mu_\gamma$  is the reduced mass corresponding to the state  $\gamma$  and the subscript  $n$  is a sequential number that labels all possible combinations of the quantum numbers  $\{\gamma, \ell, s\}$  (see Table 1).

If we do not monitor the spin states, then the total cross section for the transition from the initial internal state  $\gamma$  of the colliding particles to the final state  $\gamma'$  (the final particles can be different from the initial ones) is given by

$$\sigma(\gamma' \leftarrow \gamma) = \sum_{J \ell' s' \ell s} \sigma^J(\gamma' \ell' s' \leftarrow \gamma \ell s) . \quad (11)$$

### 2.3 Analytic properties

The Jost matrices (and thus the  $S$ -matrix) are not single-valued functions of the energy. There are two reasons for this:

- The in-coming and out-going spherical waves (3), and thus their amplitudes,  $f^{(\text{in/out})}(E)$ , depend on  $E$  via all the channel momenta;
- For charged particles, there is an additional complication, namely, the in-coming and out-going spherical waves (and thus their amplitudes) depend on  $\ln(k_n)$ .

For the channel momenta,

$$k_n = \pm \sqrt{\frac{2\mu_n}{\hbar^2}(E - E_n)} , \quad n = 1, 2, \dots, N , \quad (12)$$

where  $E_n$  are the threshold energies, there are  $2^N$  possible combinations of the signs in front of the  $N$  square roots (12). Therefore for each value of the energy the Jost matrix has  $2^N$  different values.

The complex function  $\ln(k_n)$  has infinitely many different values,

$$\ln(k_n) = \ln \{ |k_n| e^{i[\arg(k_n) + 2\pi m]} \} = \ln |k_n| + i \arg(k_n) + i2\pi m, \quad m = 0, \pm 1, \pm 2, \dots, \quad (13)$$

corresponding to different choices of  $m$ . It is defined on the “spiral” Riemann surface with the branch point at  $k_n = 0$ . It is customary to define the so called principal branch of the logarithm as the part of this surface corresponding to  $m = 0$  and  $-\pi < \arg(k_n) \leq \pi$ . The value of the function  $\ln(k_n)$  in Eq. (13) corresponds to the energy

$$E - E_n = |E - E_n| \exp(i\varphi_n + i4\pi m), \quad (14)$$

where  $-2\pi < \varphi_n \leq 2\pi$  and  $\arg(k_n) = \varphi_n/2$ . Since the momentum is the square root of the energy, the interval  $-2\pi < \varphi_n \leq 0$  covers the unphysical (with respect to channel  $n$ ) Riemann sheet where  $\text{Im } k_n < 0$ , and the interval  $0 < \varphi_n \leq 2\pi$  corresponds to the physical sheet with  $\text{Im } k_n > 0$ . These two intervals are represented by the two sheets of the Riemann surface stemming from the square-root branch point. Generally speaking, each threshold energy,  $E_n$ , is a square-root and a logarithmic branch point at the same time.

In order to have a one-to-one correspondence between the energy and the set of the channel momenta and their logarithms, the multiple copies (sheets) of the energy plane are used. For each sheet the imaginary parts of all the channel momenta as well as the corresponding logarithmic indices  $m$  have definite values. Each of these sheets is cut along its own real axis from the lowest threshold to infinity. The edges of the cuts of different sheets are interconnected in such a way that the path around one or more thresholds leads to an appropriate changes of  $\text{Im } k_n$  and  $m$ . On the multi-layered Riemann surface obtained in this way, the Jost matrices (and therefore the  $S$ -matrix) are single-valued functions of the energy.

In the “simple” case, when the Coulomb potential is absent, the Jost matrices are defined on a Riemann surface consisting of  $2^N$  sheets. Apparently, the sign of  $\text{Im } k_n$  is determined by the choice of the sign in Eq. (12). The points sitting on a vertical line passing through all the sheets, correspond to the same energy but to different choices of the signs in Eqs. (12).

At each threshold (where  $k_n = 0$  and therefore the choice of the sign for  $k_n$  is immaterial) there are  $2^{N-1}$  pairs of Riemann sheets that touch each other. Moving around such a branch point, we pass from one sheet to the other and back, because the sign of the corresponding channel momentum changes to the opposite after one full circle. For a single-channel case ( $N = 1$ ), such a Riemann surface is schematically shown in Fig. 1.

When a Coulomb potential is present, the first full circle around the branch point changes the sign of  $\text{Im } k_n$ , while the second full circle brings back the original sign but also increases (anti-clockwise direction) or decreases (clockwise direction)  $m$  in Eq. (13) by one unit. This means that moving in the same direction (clockwise or anti-clockwise), we can never come back to the same sheet. For the single-channel case, this is illustrated in Fig. 2.

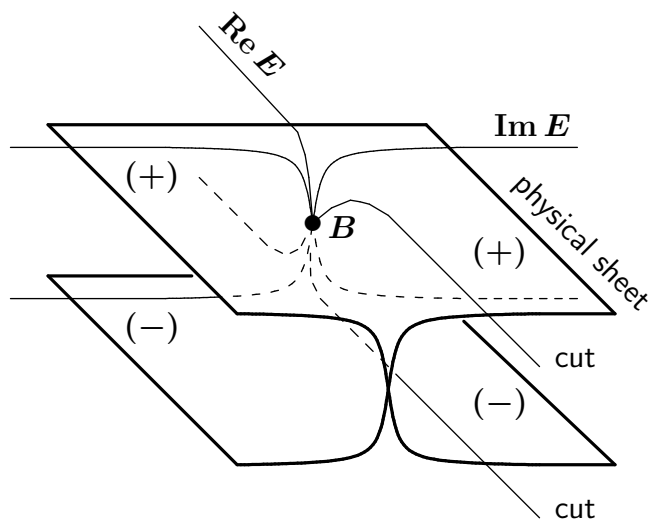


Figure 1: Fragments of the physical (+) and unphysical (-) sheets of a single-channel Riemann surface around the branch point ( $B$ ) that corresponds to the threshold energy  $E_1 = 0$ . Each sheet has its own real and imaginary axes, and the point  $B$  is their common zero-point. Transition from (+) to (-) and back is possible through the cuts of both sheets, running from  $B$  to infinity along positive half of the corresponding real axes.



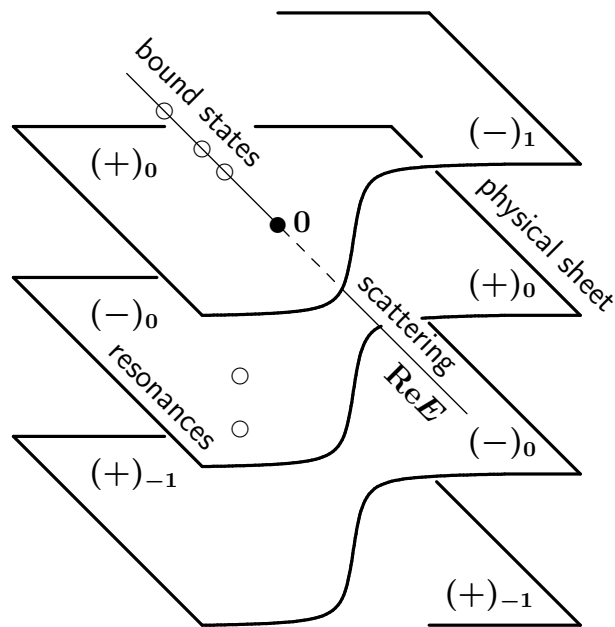


Figure 2: Spiral Riemann surface for a single-channel potential with a Coulomb tail. The symbols  $(\pm)_m$  label the sheets where  $\text{Im}(k)$  is either positive or negative, and the subscript  $m$  is the number of  $i2\pi$  in Eq. (13) stemming from the logarithmic branching.

The sheet of the Riemann surface where  $\text{Im } k_n > 0$  is called physical sheet with respect to the channel  $n$ . Otherwise it is called non-physical with respect to that channel. The scattering energies are on the upper rim of the cut of the sheet that is physical with respect to all the channels. The resonances are the discrete points (where the  $S$ -matrix is singular) on the sheet that is non-physical with respect to all open channels. This is because the open-channel components of the resonance wave functions asymptotically behave as pure outgoing divergent spherical waves, and this is only possible if  $\text{Im } k_n < 0$  for all  $n$  corresponding to the open channels.

In addition to the bound-state and resonance spectral points, the multi-channel  $S$ -matrix may have poles at “wrong” locations on the Riemann surface, i.e. where the corresponding wave function asymptotically does not behave “correctly”. Such solutions of the Schrödinger equation have no physical meaning. However, mathematically these “wrong” poles may influence the behaviour of the  $S$ -matrix at the physical scattering energies, if they are close enough to the real axis passing through the physical sheet. Such singular points are called the “shadow” poles of the  $S$ -matrix. Apparently, if such a shadow pole has an influence on the observable quantities, it cannot be ignored, but (in contrast to the resonances) the imaginary part of the corresponding energy cannot be interpreted as a width of a decay process (because the corresponding wave function has wrong asymptotic behaviour).

As is seen, the Coulomb forces drastically change the Riemann surface. However, we can safely ignore all the sheets with  $m \neq 0$ , because any possible  $S$ -matrix poles on them are far away from the upper rim of the real axis on the physical sheet  $(+)_0$ , where the scattering takes place, and thus such poles would have no influence. The sheets with  $m = 0$  correspond to the so-called principal branch of the logarithm function and therefore can be called principal sheets of the Riemann surface. The only thing that should not be forgotten is that, in contrast to Fig. 1, it is not possible to pass from  $(+)_0$  to  $(-)_0$  when moving in the anti-clockwise direction. In other words, with the presence of a Coulomb potential the principal sheets of the Riemann surface are not all interconnected among themselves.

In the present paper we deal with a two-channel problem, where there is no Coulomb potential in the first channel ( $n\alpha$ ), but it is present in the second one ( $dt$ ). The corresponding Riemann surface is shown in Fig. 3. There are four ( $2^N$ ) principal sheets, namely,  $(++)_0$ ,  $(+-)_0$ ,  $(-+)_0$ , and  $(--)_0$ , where the subscript indicates the value of  $m$  in Eq. (13) for the second channel. The cuts between  $E_1$  and  $E_2$  are interconnected as for the neutral particles. The logarithmic branch point is at the second threshold, beyond which the sheets have the spiral interconnections. Of course there are infinite number of the sheets at any energy. For the low energies, they are the direct extensions of all the spiral sheets shown for  $E > E_2$ . However, in order to reach them from the low energies, we have to go around the branch point at  $E_2$ . As was already mentioned, we can ignore them because the behaviour of the Jost matrices on them cannot affect any observable quantities.

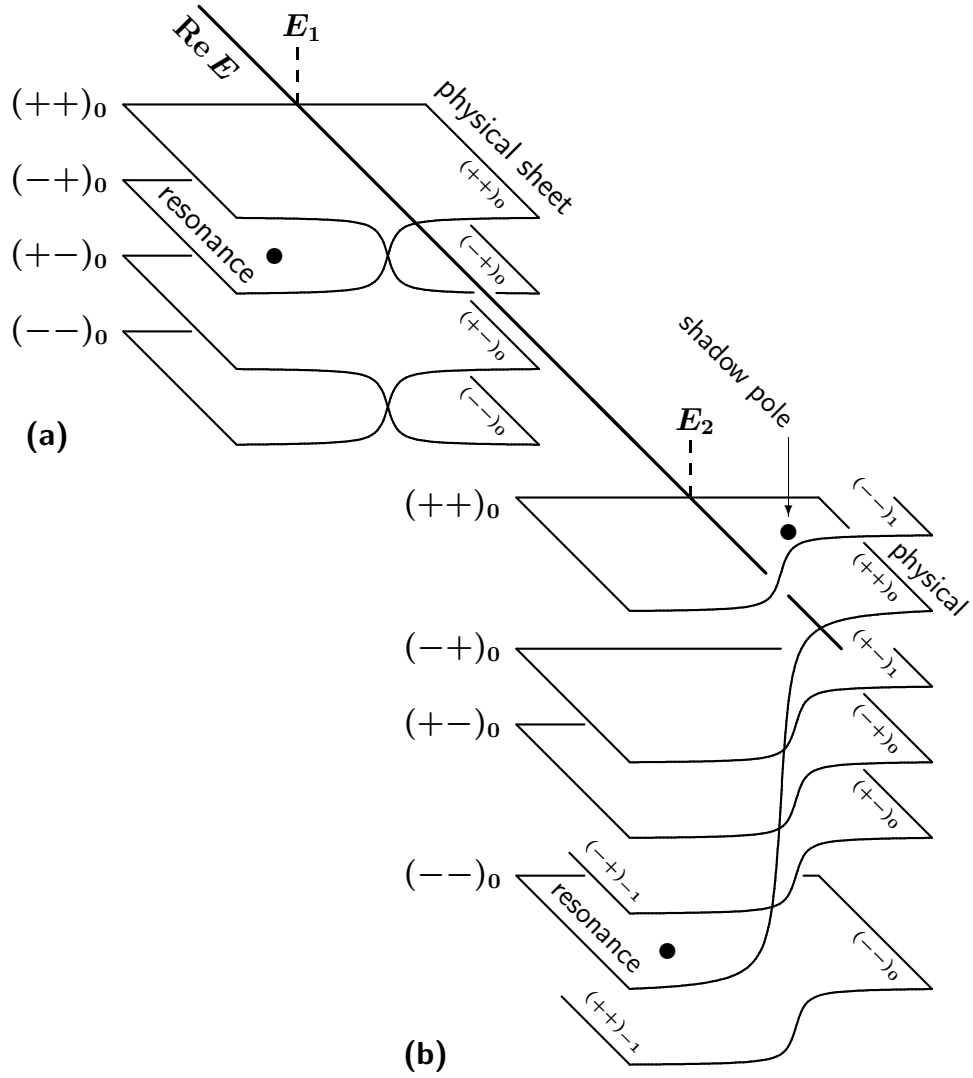


Figure 3: Interconnections of the Riemann sheets for the two-channel problem, where the Coulomb potential is only present in the second channel: (a) the interconnections between the thresholds  $E_1$  and  $E_2$ ; (b) the interconnections above the highest threshold. The symbols  $(\pm\pm)_m$  label the sheets where  $\text{Im}(k_1)$  and  $\text{Im}(k_2)$  are either positive or negative, and the subscript  $m$  is the number of  $i2\pi$  in Eq. (13) for the second channel.

## 2.4 Analytic structure

It is seen that even in the simple two-channel case the Riemann surface has a very complicated topology. Therefore when doing an analytic continuation of the Jost matrix (or the  $S$ -matrix) from the real axis to complex energies, one should be careful. This is especially true when such a continuation is done near a branch point (i.e. near a threshold energy).

Very often the  $S$ -matrix is defined with additional square roots of the channel momenta (see, for example, Ref. [24]),

$$\tilde{S}_{n'n} = \sqrt{k_{n'}} \sum_{n''} f_{n'n''}^{(\text{out})} [f_{n''n}^{(\text{in})}]^{-1} \frac{1}{\sqrt{k_n}}, \quad (15)$$

and with the corresponding re-definition of the reaction amplitude (9),

$$f_{n' \leftarrow n}^J = \frac{\tilde{S}_{n'n}^J - \delta_{n'n}}{2i\sqrt{k_{n'}k_n}} i^{\ell_n - \ell_{n'}}. \quad (16)$$

Such a definition makes the  $S$ -matrix symmetric and unitary on the real axis. This is convenient, but the price one has to pay for such a convenience is the uncertainty when matrix  $\tilde{S}(E)$  is continued to complex energies in search for resonances. Indeed, the root of the fourth order,  $\sqrt{k_n} \sim \sqrt[4]{E - E_n}$ , of a complex number has four different values. For example  $\sqrt[4]{1}$  is equal either to  $\pm 1$  or to  $\pm i$ . In other words, each threshold  $E_n$  becomes a fourth-order branch point ( $\sqrt[4]{E - E_n}$ ) instead of the second order ( $\sqrt{E - E_n}$ ). As a result the number of the Riemann sheets is artificially increased. The same difficulty shows up when the so called  $K$ -matrix is used for the analytic continuation. We do not claim that using the matrix (15) always leads to wrong analytic continuation, but one should be extremely careful, especially when doing numerical calculations because different compilers work with the complex numbers and with multi-valued functions differently.

In our approach, neither Eq. (8) nor Eq. (15) is used for the analytic continuation. We do the continuation of the Jost matrix that does not involve any additional square roots of the momenta. Moreover, we use special semi-analytic representation of the Jost matrices suggested in Refs. [19, 20], where the factors responsible for the branching of the Riemann surface are given explicitly. It was shown [20] that the Jost matrices have the following structure

$$\begin{aligned} f_{mn}^{(\text{in/out})}(E) &= \frac{e^{\pi\eta_m/2}\ell_m!}{\Gamma(\ell_m + 1 \pm i\eta_m)} \left\{ \frac{C_{\ell_n}(\eta_n)k_n^{\ell_n+1}}{C_{\ell_m}(\eta_m)k_m^{\ell_m+1}} A_{mn}(E) - \right. \\ &\quad \left. - \left[ \frac{2\eta_m h(\eta_m)}{C_0^2(\eta_m)} \pm i \right] C_{\ell_m}(\eta_m) C_{\ell_n}(\eta_n) k_m^{\ell_m} k_n^{\ell_n+1} B_{mn}(E) \right\}, \end{aligned} \quad (17)$$

where the matrices  $\mathbf{A}(E)$  and  $\mathbf{B}(E)$  are single-valued functions of  $E$ , defined on a simple  $E$ -plane without any branch points. These matrices are the same for both  $\mathbf{f}^{(\text{in})}$  and  $\mathbf{f}^{(\text{out})}$ . It was also shown that for real energies the matrices  $\mathbf{A}(E)$  and  $\mathbf{B}(E)$  are real.

Eq. (17) gives us the Jost matrices in the semi-analytic form, where the matrices  $\mathbf{A}$  and  $\mathbf{B}$  are unknown, but are simple and single-valued, while all the troublesome factors (that are responsible for the branching) are given explicitly. They involve the Coulomb barrier factor  $C_\ell$  and the function  $h(\eta)$  associated with the Coulomb potential<sup>1</sup>:

$$C_\ell(\eta) = \frac{2^\ell e^{-\pi\eta/2}}{(2\ell)!!} \exp \left\{ \frac{1}{2} [\ln \Gamma(\ell + 1 + i\eta) + \ln \Gamma(\ell + 1 - i\eta)] \right\} \xrightarrow{\eta \rightarrow 0} 1, \quad (18)$$

$$h(\eta) = \frac{1}{2} [\psi(i\eta) + \psi(-i\eta)] - \ln \eta, \quad \psi(z) = \frac{\Gamma'(z)}{\Gamma(z)}, \quad \eta = \frac{e^2 Z_1 Z_2 \mu}{\hbar^2 k}. \quad (19)$$

For neutral particles (when  $\eta = 0$ ), Eq. (17) becomes more simple [19],

$$\mathbf{f}_{mn}^{(\text{in/out})}(E) = \frac{k_n^{\ell_n+1}}{k_m^{\ell_m+1}} A_{mn}(E) \mp i k_m^{\ell_m} k_n^{\ell_n+1} B_{mn}(E). \quad (20)$$

It should be noted that the analytic structure of the  $S$ -matrix is much more complicated than that of the Jost matrices. This becomes obvious if we substitute the matrices (17) in Eq. (8). It is therefore more simple to deal with  $\mathbf{f}^{(\text{in/out})}(E)$ , when doing the analytic continuation from real to complex  $E$ . If the  $S$ -matrix itself is used for such a task, and especially when such a matrix is constructed in a simplified phenomenological way, it is difficult to guarantee that the continuation is done to the correct sheet of the Riemann surface.

## 2.5 Approximation and analytic continuation

The unknown matrices  $\mathbf{A}(E)$  and  $\mathbf{B}(E)$  in the semi-analytic representations (17) and (20) are single-valued and analytic. This means that they can be expanded in Taylor series around an arbitrary complex energy  $E_0$ ,

$$\mathbf{A}(E) = \mathbf{a}^{(0)} + \mathbf{a}^{(1)}(E - E_0) + \mathbf{a}^{(2)}(E - E_0)^2 + \dots, \quad (21)$$

$$\mathbf{B}(E) = \mathbf{b}^{(0)} + \mathbf{b}^{(1)}(E - E_0) + \mathbf{b}^{(2)}(E - E_0)^2 + \dots, \quad (22)$$

where  $\mathbf{a}^{(m)}(E_0)$  and  $\mathbf{b}^{(m)}(E_0)$  are the  $(N \times N)$ -matrices depending on the choice of the center  $E_0$  of the expansion. These matrices consist of unknown parameters. Taking the first several

---

<sup>1</sup>The logarithmic branching stems from the function  $h(\eta)$ .

terms of these expansions and finding the parameters  $\mathbf{a}^{(m)}$  and  $\mathbf{b}^{(m)}$  via fitting some available experimental data, we can obtain approximate analytic expressions (17) for the Jost matrices.

Since the matrices  $\mathbf{A}(E)$  and  $\mathbf{B}(E)$  are real for real energies, it is convenient to choose  $E_0$  on the real axis. As a result the parameters  $\mathbf{a}^{(m)}$  and  $\mathbf{b}^{(m)}$  are also real. If they were complex then the number of the fitting parameters would double (their real and imaginary components are independent parameters).

Although  $E_0$  is on the real axis, the expansions (21,22) are valid for complex  $E$  within a circle around  $E_0$ . After finding the fitting parameters  $\mathbf{a}^{(m)}$  and  $\mathbf{b}^{(m)}$ , we can use the analytic expression (17) for the Jost matrix  $\mathbf{f}^{(\text{in})}(E)$ , to locate the resonances as the roots of Eq. (7) at complex energies. When doing this, we can choose the appropriate sheet of the Riemann surface. The single-valued functions  $\mathbf{A}(E)$  and  $\mathbf{B}(E)$  are the same on all the sheets. The differences only stem from the explicit factors depending on  $k_n$  in Eq. (17).

When the energy  $E$  is given, in order to choose a specific sheet, we calculate the square roots (12) for all the channel momenta and check the signs of their imaginary parts. If for a particular  $k_n$  the sign of  $\text{Im } k_n$  is not right, we simply replace  $k_n$  with  $-k_n$ . After getting all the channel momenta with the appropriate signs, we calculate the Jost matrices as is given by Eq. (17). Since in this equation all the factors depending on the choice of the signs, are given in an exact way, we are sure that despite the approximations (21,22), the Jost matrices are calculated just for a chosen sheet of the Riemann surface. In other words, the analytic continuation of the Jost matrices from the real axis (where the fitting is done) to a chosen Riemann sheet is always done correctly.

Looking at the expansions (21,22), which we truncate at certain number of terms, one might think that we work with a polynomial approximation of the reaction cross section. However, since the  $S$ -matrix is a “ratio” (8) of the Jost matrices, our approximation is more similar to the Padé approximation [26]. It is well known that the Padé approximants, which are ratios of two polynomials, are more accurate and efficient than any polynomial ones, because they include some complex poles that influence the behaviour of the function on the real axis. In our approach, each element of the  $S$ -matrix is a ratio of two functions. They are not just polynomials but some more complicated functions. For all the elements, the denominator is the same, namely,  $\det \mathbf{f}^{(\text{in})}(E)$ . Our approximation is better than the Padé one because it involves not only the poles but also the correct factors determining the branching of the Riemann surface.

### 3 The data to fit

The unstable system  ${}^5\text{He}$  has been studied for many years. There is an extensive list of publications [1] where the results of these studies are reported. In principle, using the approach

described in the present paper it is possible to fit any available data. Indeed, the parametrized Jost matrices give us the corresponding  $S$ -matrix, from which it is possible to calculate any observable quantity as a function of the fitting parameters. However, it would be a waste of time and effort to collect and fit the original data. Instead, we can rely on the existing  $R$ -matrix fits. In fact the  $R$ -matrix fit is the most accurate and efficient way of parametrizing a collection of scattering data.

The  $R$ -matrix is good for real energies, but its extension to complex  $E$  is questionable. This should be clear from the previous Sections of this paper, where we describe the complicated topology of the Riemann surface. The analytic continuation onto this surface is the task where our approach can complement the real energy  $R$ -matrix parametrization.

Taking an  $R$ -matrix with a given set of parameters, we calculate the partial cross sections (in certain channels) at the energies we need. Thus obtained cross sections can be considered as experimental data, which we then fit using the Jost matrices. In a sense, within such an approach the  $R$ -matrix fit serves as a “preliminary refinement” of the “raw” data. It is similar to doing the phase-shift analysis. Nobody actually measures the scattering phase shifts, but still the tables of them are considered as experimental data.

As was stated from the outset, we restrict our consideration to the resonant state of  ${}^5\text{He}$  with  $J^\pi = \frac{3}{2}^+$  near the  $dt$ -threshold. This state can only be a mixture of the four channels listed in Table 1, i.e. its wave function is a linear combination of the four individual channel wave functions. Apparently, their contributions into such a combination are different. In order to do a preliminary estimate of the importance of each of the channels in this combination, we can look at the partial cross sections defined by Eq. (10), for all (sixteen) possible mutual transitions among the four channels. This can be done using an  $R$ -matrix parametrization.

As such a parametrization, we use the comprehensive four-level four-channel  $R$ -matrix fit reported in Ref. [5]. Generated from this  $R$ -matrix, the partial cross sections for the transitions from the first, second, third, and the fourth channels, respectively, are shown in Figs. 4-7. The magnitudes of the cross sections for the transitions to different channels are so different that we have to use the logarithmic scale in order to fit them in the same figure.

As is seen, at the energies around the resonance we are studying ( $\sim 50$  keV above the  $dt$ -threshold), the probabilities of the off-diagonal transitions  $1 \leftrightarrow 3$ ,  $1 \leftrightarrow 4$ ,  $2 \leftrightarrow 3$ ,  $2 \leftrightarrow 4$ , and  $3 \leftrightarrow 4$  are at least five orders of magnitude smaller than those for the diagonal ones. They also are several orders of magnitude smaller than the transition probabilities between the first and the second channels. Coming back to Table 1, it is not difficult to qualitatively explain some of these differences.

Indeed, in the first channel there is only the centrifugal barrier with  $\ell = 2$ , which is not an obstacle at the  $n\alpha$ -collision energy  $\sim 18$  MeV. The neutron and the  $\alpha$ -particle can easily come close to each other and form the compound resonant state. When this state decays, the fragments  $n$  and  $\alpha$  can easily escape through that centrifugal barrier.

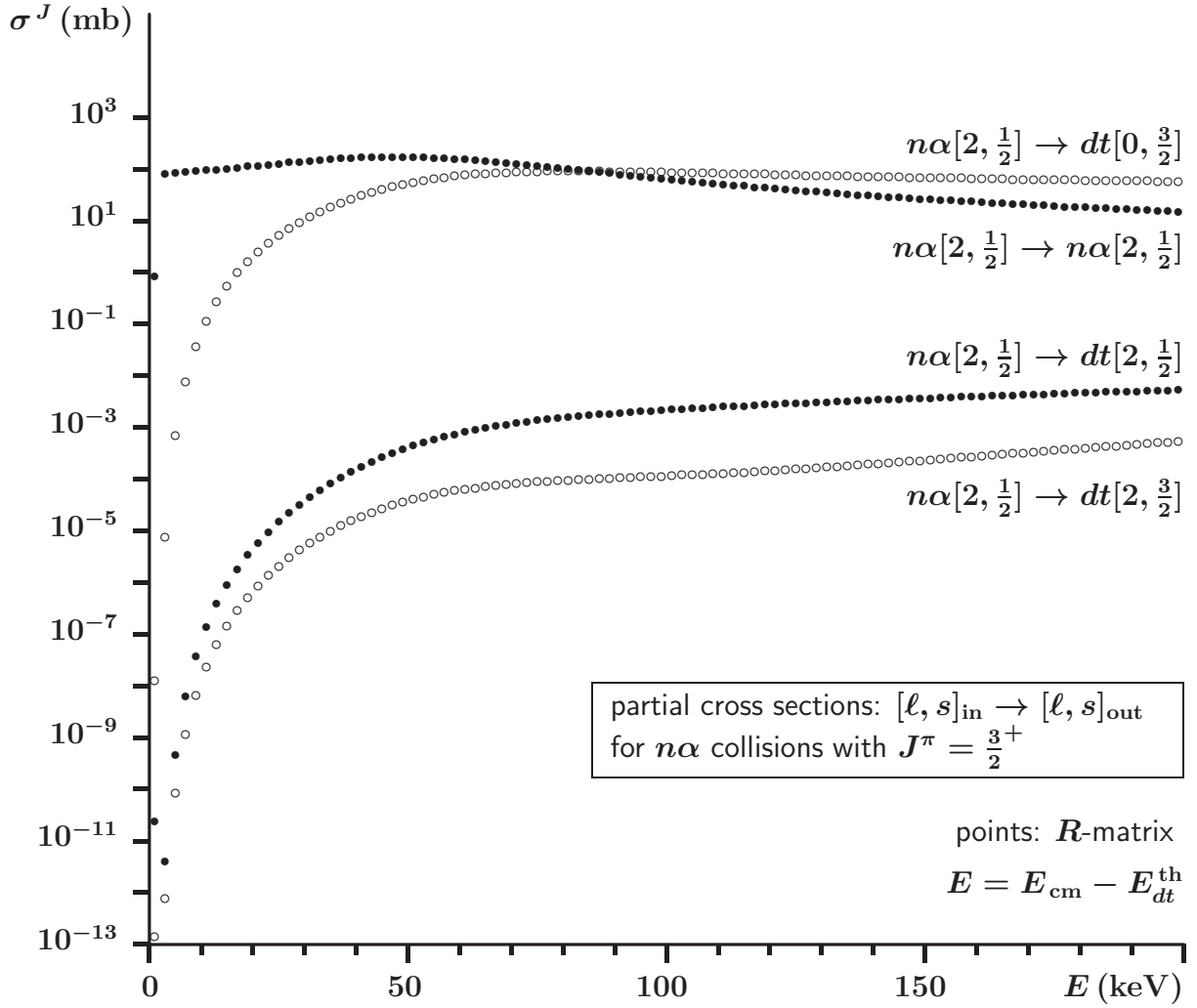


Figure 4: Partial cross sections for the channels  $1 \rightarrow 1$ ,  $1 \rightarrow 2$ ,  $1 \rightarrow 3$ , and  $1 \rightarrow 4$  as is denoted in Table 1.



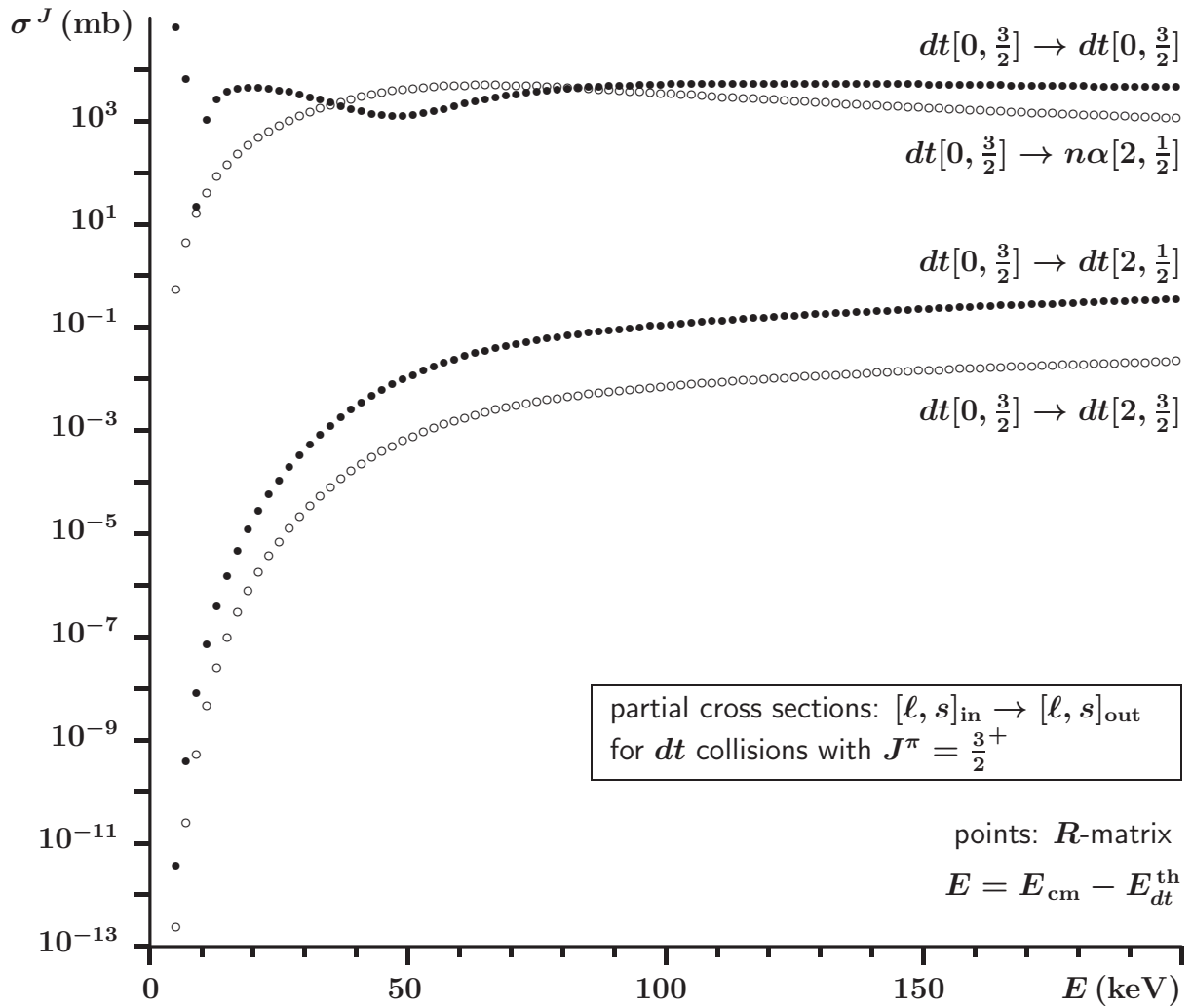


Figure 5: Partial cross sections for the channels  $2 \rightarrow 1$ ,  $2 \rightarrow 2$ ,  $2 \rightarrow 3$ , and  $2 \rightarrow 4$  as is denoted in Table 1.

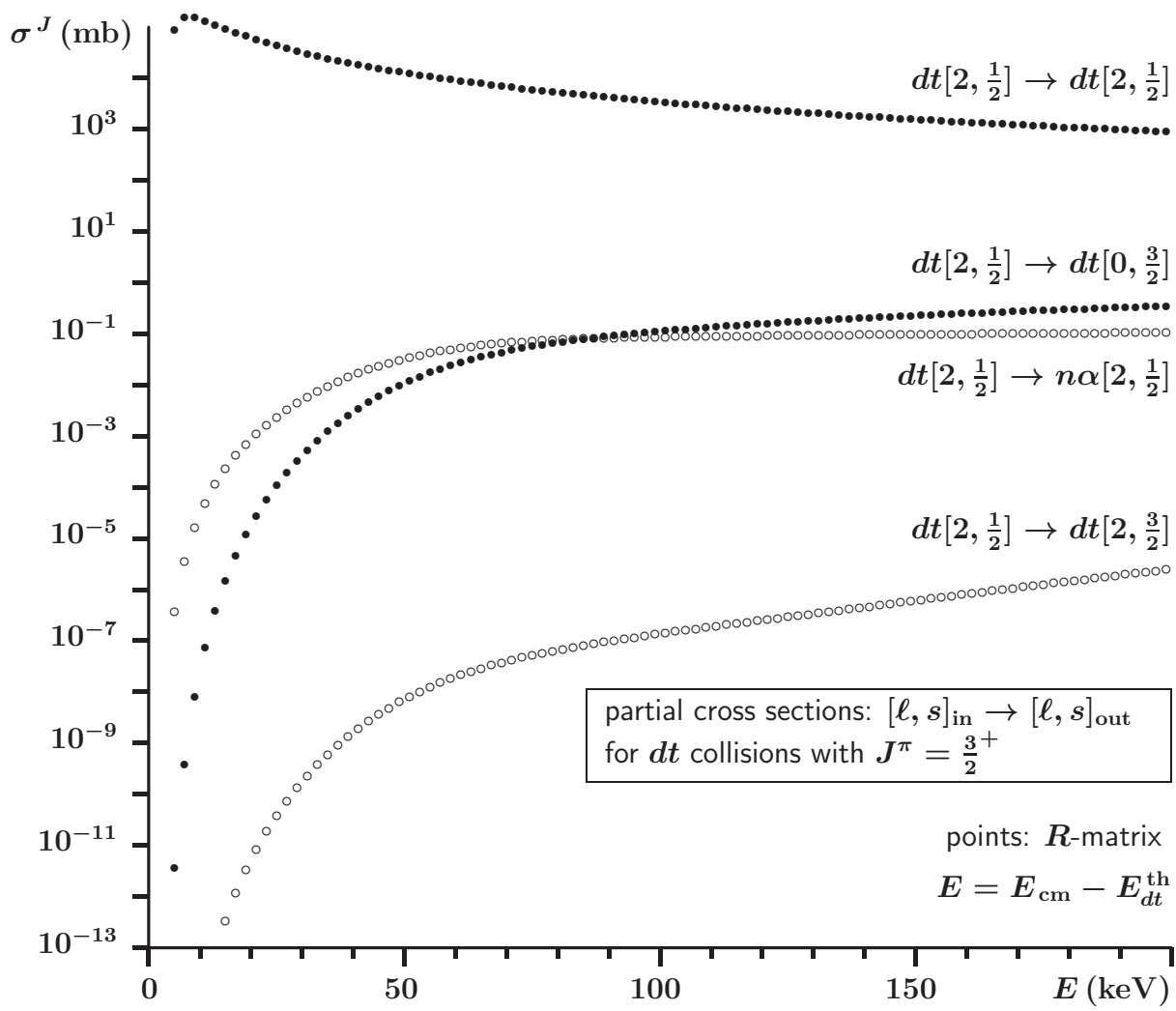


Figure 6: Partial cross sections for the channels  $3 \rightarrow 1$ ,  $3 \rightarrow 2$ ,  $3 \rightarrow 3$ , and  $3 \rightarrow 4$  as is denoted in Table 1.

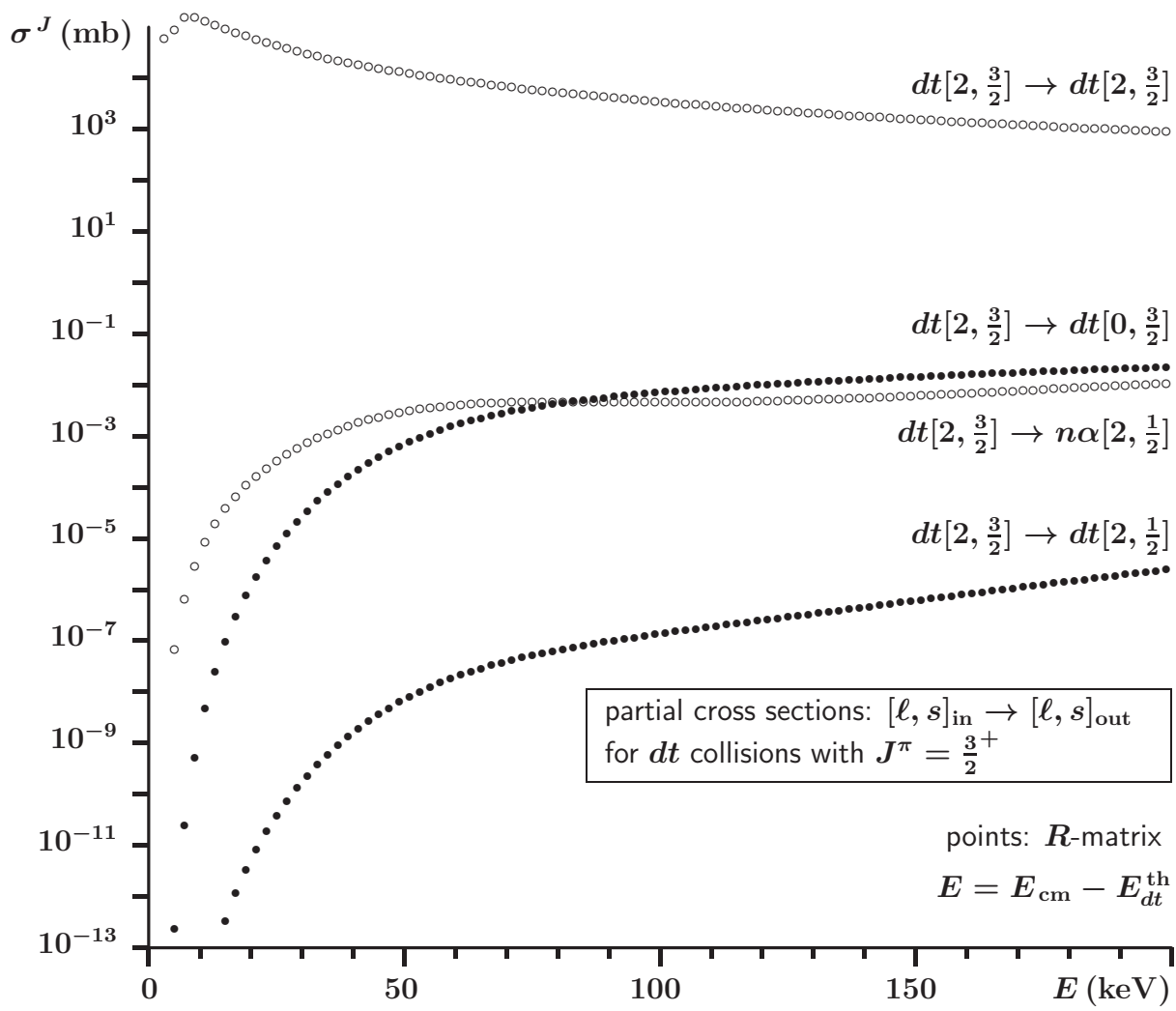


Figure 7: Partial cross sections for the channels  $4 \rightarrow 1$ ,  $4 \rightarrow 2$ ,  $4 \rightarrow 3$ , and  $4 \rightarrow 4$  as is denoted in Table 1.

The second channel ( $dt$  with  $\ell = 0$ ) has only the Coulomb barrier. The deuteron and triton still can penetrate through it to form the resonance and then to escape from it. However the relative  $dt$ -energy is much lower than in the first channel and thus the channel 2 should have a weaker coupling with the resonance. In particular, the partial decay width into this channel should be smaller than the width for the  $n\alpha$ -channel (we will see a quantitative confirmation of this intuitive reasoning in Sec. 5).

The channels 3 and 4 have the sum of both the centrifugal and the Coulomb barriers. When the  $dt$ -system is in one of these channels and the energy is around  $\sim 50$  keV, the penetration probability for the total barrier is too small. This implies that the couplings of these channels with the resonance are extremely weak.

The channels can couple to each other either via the compound resonance or via the direct reactions of the pick-up and stripping of the proton. As we see, the resonance can only couple the channels 1 and 2. In a direct reaction the transferred proton has to tunnel through the same barriers, which means that for the channels 3 and 4 such a process is also extremely improbable. The same conclusion can be found, for example, in Ref. [27].

In Figs. 6 and 7 it is seen that the transitions  $3 \leftrightarrow 4$  have the cross sections  $\sim 10^{-7}$  mb (the smallest of all the inter-channel transitions). This cannot be explained as in the above, because the barriers for these channels are the same. We do not have any reasonable explanation why the spin state  $1/2$  does not “want” to transit to the state  $3/2$  and vice versa. But this is the result of the  $R$ -matrix fit of the experimental data. We therefore simply accept as a fact that the channels 3 and 4 are practically not coupled to each other.

Summarizing the above reasoning, we conclude that the channels 1 and 2 are strongly coupled with each other, while the channels 3 and 4 are not coupled to any other channels and can be treated individually,

$$\begin{array}{ccc}
 n\alpha \left(2, \frac{1}{2}\right) & & n\alpha \left(2, \frac{1}{2}\right) \\
 & \swarrow \quad \searrow & \\
 & \text{O} & \\
 & \nwarrow \quad \nearrow & \\
 dt \left(0, \frac{3}{2}\right) & & dt \left(0, \frac{3}{2}\right)
 \end{array} , \tag{23}$$

$$dt \left(2, \frac{1}{2}\right) \longrightarrow dt \left(2, \frac{1}{2}\right) , \tag{24}$$

$$dt \left(2, \frac{3}{2}\right) \longrightarrow dt \left(2, \frac{3}{2}\right) . \tag{25}$$

This means that our original four-channel problem (as is given in Table 1) is divided in a two-channel problem (coupled channels 1 and 2) and two single-channel problems (channels 3 and 4). Of course this is an approximation, but the extremely small inter-channel cross

sections connecting the channels (1,2) with 3 and 4, allow us to ignore them. These cross sections are at least five orders of magnitude smaller than those we take into account. This is beyond the accuracy of our calculations.

## 4 Fitting procedure

The method for fitting the experimental data with the parametrized Jost matrices was tested on several single-channel and two-channel model-problems [28, 29], where the exact locations of resonances were known. It was demonstrated that the method is stable and reliable. It works equally well in the problems for neutral and for charged particles. The procedure we use here is basically the same.

The matrices  $\mathbf{A}(E)$  and  $\mathbf{B}(E)$  in Eq. (17), which are analytic and single-valued functions of the energy, are approximated by the  $(M + 1)$  Taylor terms,

$$A_{n'n}(E) \approx \sum_{m=0}^M a_{n'n}^{(m)}(E - E_0)^m, \quad (26)$$

$$B_{n'n}(E) \approx \sum_{m=0}^M b_{n'n}^{(m)}(E - E_0)^m, \quad n', n = 1, 2, \dots, N, \quad (27)$$

where  $a_{n'n}^{(m)}$  and  $b_{n'n}^{(m)}$  are the fitting parameters and  $N = 2$  is the number of the coupled channels. The Jost matrices (17) with these  $\mathbf{A}$  and  $\mathbf{B}$  are then used to calculate the  $S$ -matrix (8) and the approximate partial cross sections (10),  $\tilde{\sigma}_{n'\leftarrow n}$ , which thus depend on the fitting parameters.

In order to find the optimal values of the fitting parameters, we minimize the following  $\chi^2$ -function

$$\chi^2 = \sum_{n', n=1}^N \sum_{i=1}^K |\tilde{\sigma}_{n'\leftarrow n}(E_i) - \sigma_{n'\leftarrow n}(E_i)|^2, \quad (28)$$

where  $K$  is the number of experimental points taken into account for each partial cross section, and  $\sigma_{n'\leftarrow n}(E_i)$  is the corresponding experimental cross section at the energy  $E_i$ . Since the experimental data are taken from the  $R$ -matrix analysis, the experimental errors are not defined. We therefore put all of them to unity in the  $\chi^2$ -function (28).

The minimization is done using the MINUIT program developed in CERN [30]. The function (28) has many local minima. In order to find the best of them, we repeat the procedure many times ( $\sim 1000$ ) with randomly chosen starting values of the parameters. After a good minimum is found, we refine it by choosing random starting point around the

best point found in the parameter space. After each improvement, we do the random choice of the starting parameters around the new best point.

It should be noted that the observables are expressed via the elements of the  $S$ -matrix (8), which is the ratio of the Jost matrices. This means that any common factor in  $\mathbf{f}^{(\text{in})}$  and  $\mathbf{f}^{(\text{out})}$  cancels out in the  $S$ -matrix. Therefore the set of the parameters  $a_{n'n}^{(m)}$  and  $b_{n'n}^{(m)}$  can be scaled by any convenient factor. This does not affect any results. For example, one of the parameters can be put to a fixed value, which reduces their number in one parameter, from  $2(M+1)N^2$  to  $2(M+1)N^2 - 1$ .

## 5 Results

The two-channel ( $N = 2$ ) data (obtained from the  $R$ -matrix given in Ref. [5]) for the four processes (23) were fitted as is described in Sec. 4 with  $M = 4$  and  $E_0 = 50$  keV (the energy is counted from the  $dt$ -threshold). The results of the fit are graphically shown in Figs. 8, 9, 10, and 11.

This fit was achieved with the set of parameters given in Table 2. The units for the parameters are chosen in such a way that the Jost matrices are dimensionless.

As is seen, in Eq. (17) different matrix elements of the Jost matrices may involve different powers of the channel momenta (in the explicit factors). As a result, the units of  $A_{n'n}$  or  $B_{n'n}$  for different subscripts are different as well. To avoid this, we can always replace the channel momenta  $k_n$  in this equation with the product  $k_n R$  with an arbitrarily chosen radius  $R$ . Since the matrices  $\mathbf{A}$  and  $\mathbf{B}$  are unknown, the thus appearing additional constant factors (powers of  $R$ ) can be included in  $\mathbf{A}$  and  $\mathbf{B}$ . Such an inclusion cannot change their analytic properties, namely, the fact that they are single-valued functions of the energy. For us it is convenient to choose  $R = 1$  fm.

The single-channel data (obtained from the  $R$ -matrix given in Ref. [5]) for the processes (24) and (25) were fitted in the same way with  $M = 4$  and  $E_0 = 50$  keV. The results of the fit are graphically shown in Figs. 12 and 13, and the corresponding parameters are given in Table 3. The much larger values of these  $D$ -wave cross sections as compared to the  $S$ -wave ones shown in Fig. 11, may cause a confusion. It is therefore worthwhile to add some explanations concerning these elastic cross sections.

They are the partial cross sections integrated over all the scattering angles. Usually, the differential cross section for the charged particles is given as the absolute square of the sum of the pure Coulomb and the nuclear amplitudes. The Coulomb amplitude is infinite in the forward direction. The integrated cross section is therefore infinite as well. As a consequence, the partial wave decomposition of the pure Coulomb amplitude does not converge. However, each partial Coulomb cross section remains finite but increases with  $\ell$ . In our case, the nuclear

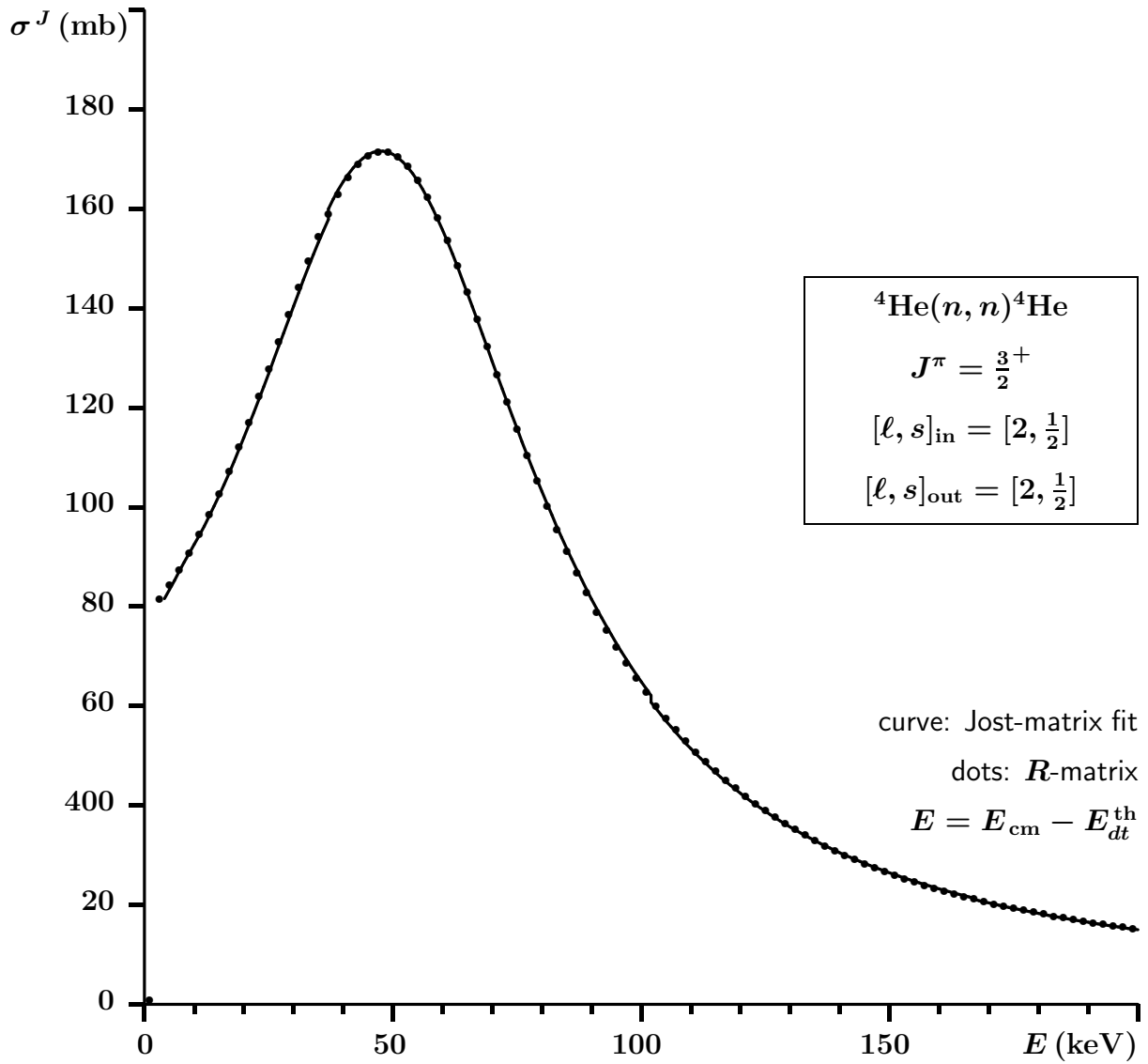


Figure 8: Fit of the partial cross section for the elastic transition  $1 \rightarrow 1$  (see the notation in Table 1).

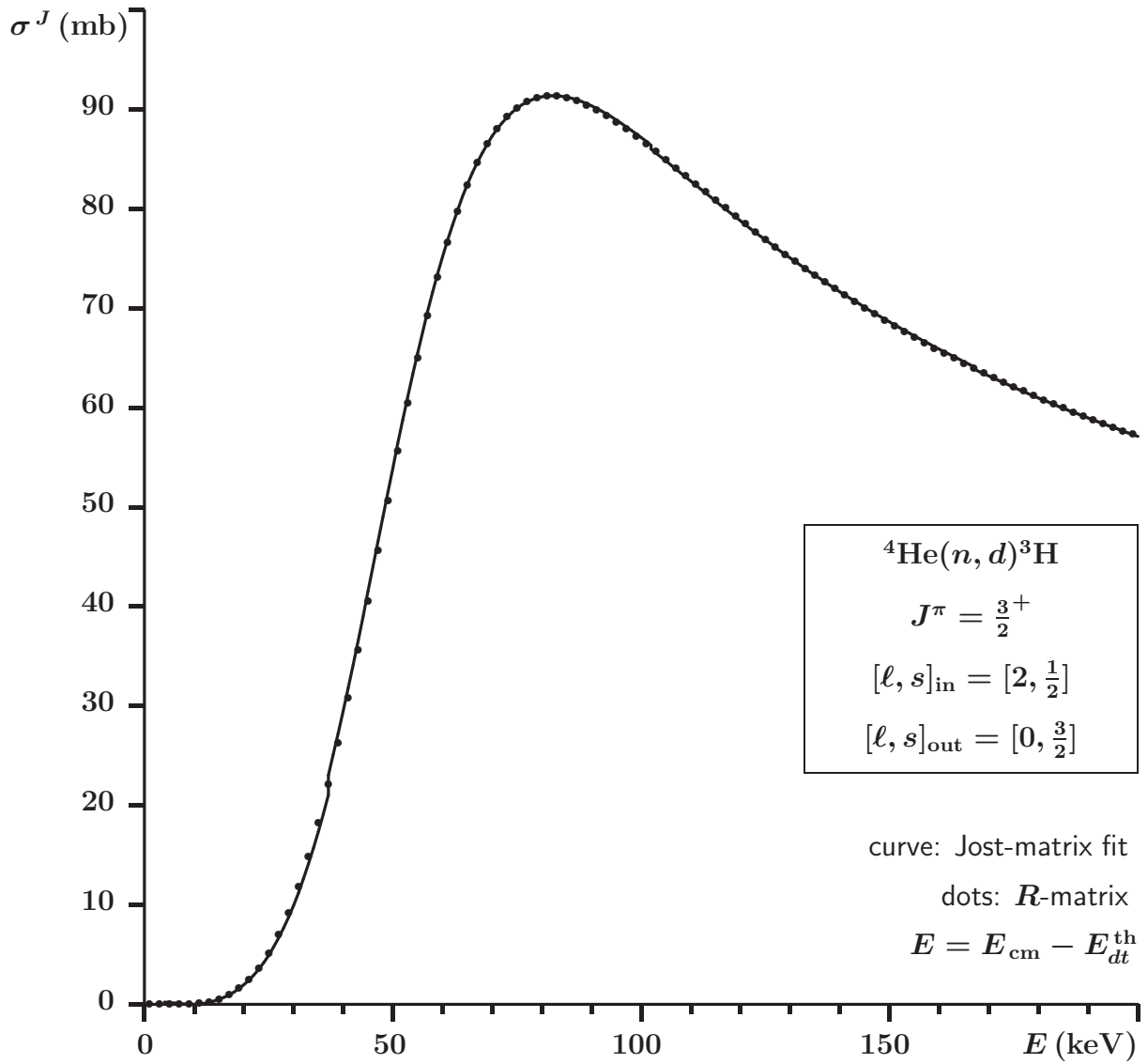


Figure 9: Fit of the partial cross section for the inelastic transition  $1 \rightarrow 2$  (see the notation in Table 1).



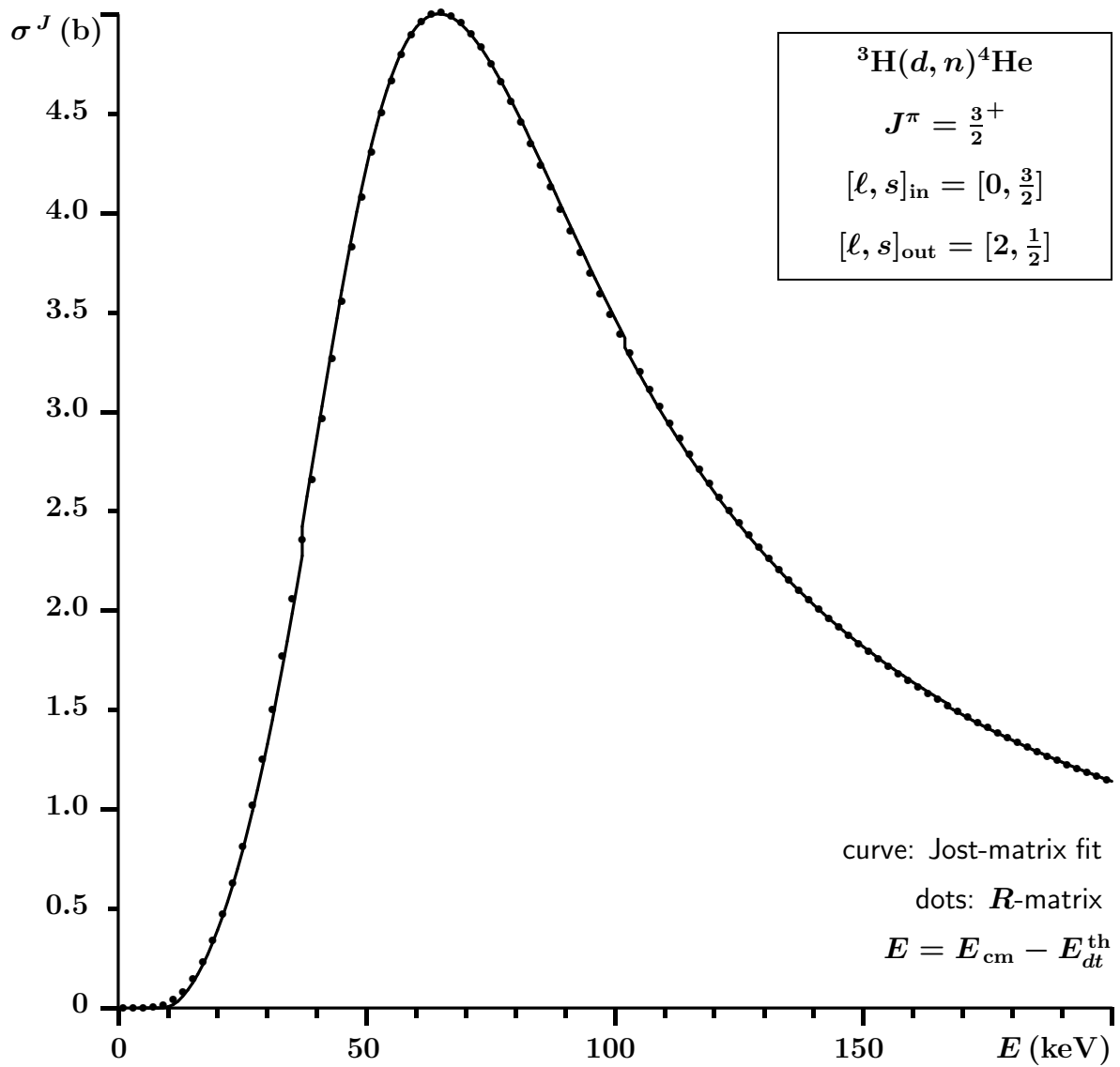


Figure 10: Fit of the partial cross section for the inelastic transition  $2 \rightarrow 1$  (see the notation in Table 1).

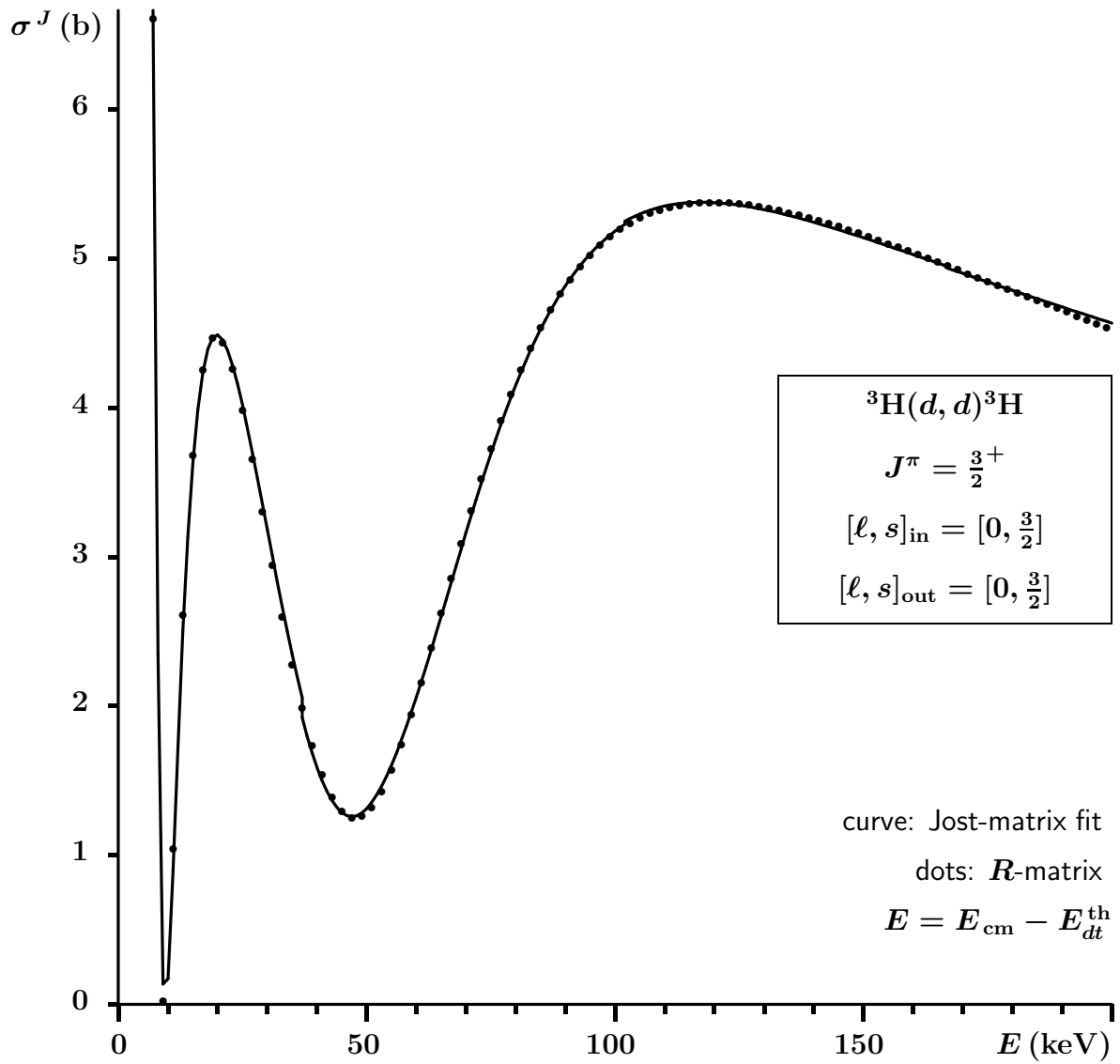


Figure 11: Fit of the partial cross section for the elastic transition  $2 \rightarrow 2$  (see the notation in Table 1).

$E_0$			40 keV	50 keV	60 keV
$m$	$n'$	$n$	$a_{n'n}^{(m)}, b_{n'n}^{(m)}$ [MeV $^{-m}$ ]	$a_{n'n}^{(m)}, b_{n'n}^{(m)}$ [MeV $^{-m}$ ]	$a_{n'n}^{(m)}, b_{n'n}^{(m)}$ [MeV $^{-m}$ ]
0	1	1	0.11653, 53.625	0.34093, 55.416	3.3788, 48.166
	1	2	1.0813, -2.1316	0.77509, -2.2752	0.57354, -2.0536
	2	1	0.96416, 32.904	0.60767, -3.9457	0.35755, -24.660
	2	2	0.057233, 4.5797	0.063612, 4.5766	0.071082, 4.4843
1	1	1	512.04, -221.91	537.08, 148.21	656.88, 410.14
	1	2	-17.408, -4.4977	-6.0448, -16.604	5.7879, -26.110
	2	1	13.264, -1127.4	8.0623, -1102.8	20.584, -1038.6
	2	2	2.4459, 96.388	2.7856, 115.63	3.1034, 124.21
2	1	1	-6457.5, 14179	10660, 15358	20237, 12090
	1	2	567.39, -705.56	733.01, -780.22	678.85, -696.52
	2	1	54.500, 30091	967.39, 11746	1699.3, 2380.9
	2	2	36.874, 1314.1	57.122, 1841.8	66.282, 2116.1
3	1	1	737310, 29257	659610, -31260	506310, -58864
	1	2	13254, -2728.6	8435.9, -3067.5	6439.0, -2442.2
	2	1	34325, -352760	47376, -94790	45900, 95653
	2	2	1082.3, 34639	1148.7, 33655	1036.4, 26021
4	1	1	3123300, -2214800	2140300, -1764300	1353200, -1201600
	1	2	119530, -37503	75737, -14863	50499, -5779.9
	2	1	774390, 11616000	565470, 9340700	373110, 6407400
	2	2	22306, 171080	12689, 56199	7858.0, 14180

Table 2: Parameters of the expansions (26,27) for the coupled channels 1 and 2 with three choices of the central point  $E_0$ . These parameters for  $E_0 = 50$  keV were used to generate the curves shown in Figs. 8, 9, 10, and 11, and to locate the resonances.

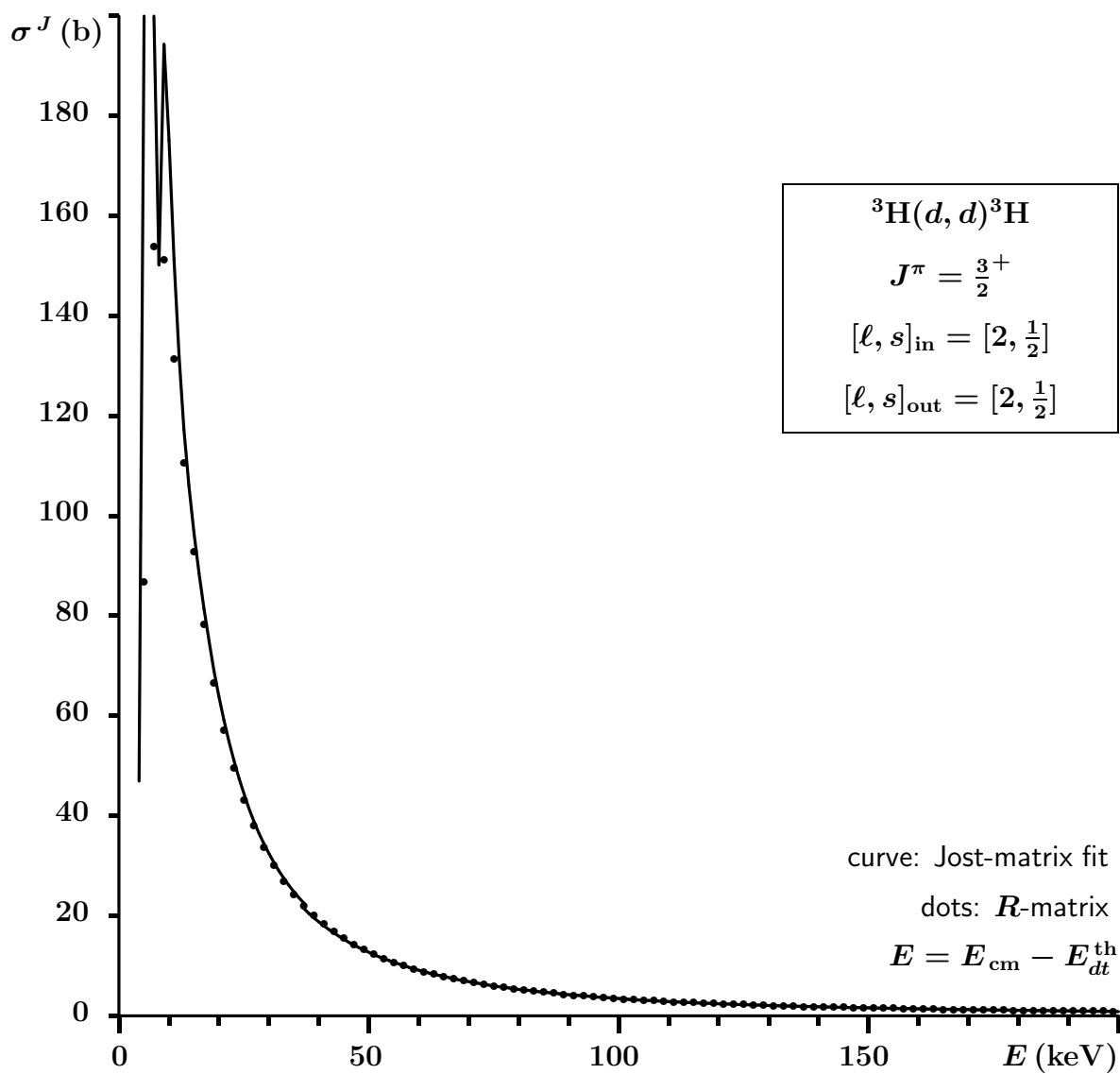


Figure 12: Fit of the partial cross section for the elastic transition  $3 \rightarrow 3$  (see the notation in Table 1).

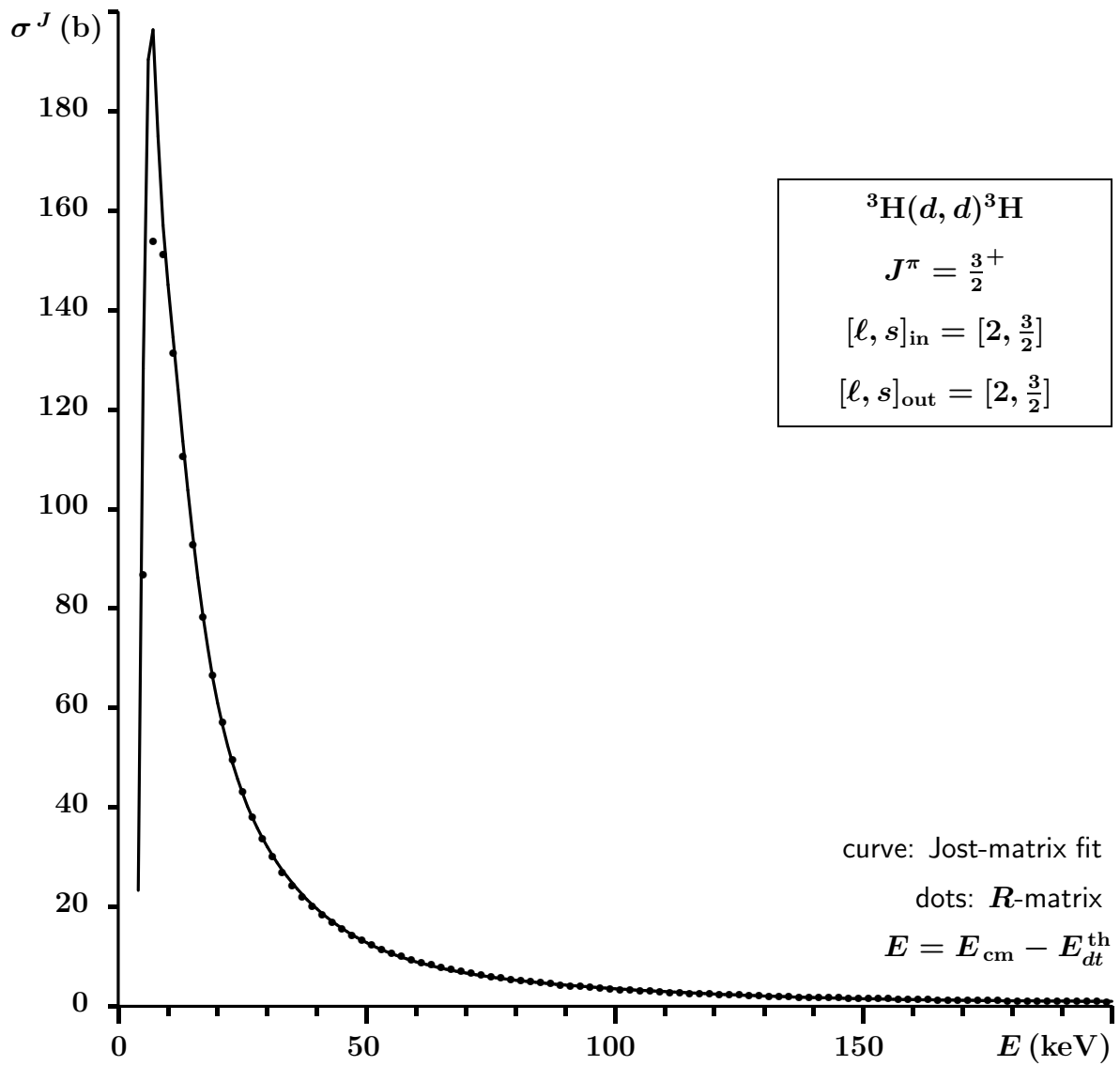


Figure 13: Fit of the partial cross section for the elastic transition  $4 \rightarrow 4$  (see the notation in Table 1).

	3 → 3	4 → 4
$m$	$a^{(m)}, b^{(m)}$ [keV $^{-m}$ ]	$a^{(m)}, b^{(m)}$ [keV $^{-m}$ ]
0	$-2.9864 \times 10^{-2}, -154870$	$-2.3603 \times 10^{-2}, -118470$
1	$-1.4516 \times 10^{-3}, -413.64$	$-1.2782 \times 10^{-3}, -872.71$
2	$-2.0099 \times 10^{-5}, -2.1701$	$-2.5236 \times 10^{-5}, -17.221$
3	$-4.2416 \times 10^{-9}, 2.0267 \times 10^{-2}$	$-2.2213 \times 10^{-7}, 9.9099 \times 10^{-2}$
4	$1.1253 \times 10^{-9}, -4.5799 \times 10^{-5}$	$-7.9892 \times 10^{-10}, -1.3967 \times 10^{-3}$

Table 3: Parameters of the expansions (26,27) with  $E_0 = 50$  keV for the (uncoupled) single channels 3 and 4. These parameters generate the curves shown in Figs. 12 and 13.

part of the partial-wave scattering amplitude is known from the  $R$ -matrix fit. By adding to it the corresponding partial-wave Coulomb amplitude and integrating over the angles, we obtain the “experimental” partial cross section (the dots in the Figures). We have to add the pure Coulomb part to the  $R$ -matrix amplitude because, these “experimental” data are then fitted using the Jost matrices where the Coulomb and nuclear contributions are not separated. The “experimental” points in Figs. 12 and 13 are higher than the points in Fig. 11 because the pure Coulomb contribution grows with the angular momentum.

When looking for resonances, we considered the Jost matrix (17) at complex energies. The zeros of its determinant were sought using the Newton’s method [26]. The choice of an appropriate sheet of the Riemann surface was done as is described in Sec. 2.5.

The partial widths for the two-channel system were determined using the method developed in Ref. [31]. Actually, they are expressed in terms of the matrix elements of the Jost matrices:

$$\Gamma_i = \frac{\text{Re}(k_i) |\mathcal{A}_i|^2 \Gamma}{\sum_{i'=1}^N \frac{\mu_i}{\mu_{i'}} \text{Re}(k_{i'}) |\mathcal{A}_{i'}|^2}, \quad (29)$$

where  $i = 1$  and  $i = 2$  correspond to the  $n\alpha$  and  $dt$  channels, and  $\mathcal{A}_1$  and  $\mathcal{A}_2$  are the asymptotic amplitudes (see Ref. [31]) of the channels, given by

$$\mathcal{A}_1 = f_{11}^{(\text{out})} - \frac{f_{11}^{(\text{in})} f_{12}^{(\text{out})}}{f_{12}^{(\text{in})}}, \quad \mathcal{A}_2 = f_{21}^{(\text{out})} - \frac{f_{11}^{(\text{in})} f_{22}^{(\text{out})}}{f_{12}^{(\text{in})}}. \quad (30)$$

In these equations the Jost matrices are taken at the complex resonant energy.

$E_r$ (keV)	$\Gamma$ (keV)	$\Gamma_{n\alpha}$ (keV)	$\Gamma_{dt}$ (keV)
9.1	9.0	7.4	1.6
50.2	46.3	29.1	17.2
62.1	92.8	76.6	16.2

Table 4: Parameters of the resonances found for the coupled channels 1 and 2 (see Table 1).

$S$ -matrix poles (keV)			
$(++)_0$	$(-+)_0$	$(+-)_0$	$(--)_0$
$9.0 - i4.6$	$9.1 - i4.6$	$9.1 - i4.5$	$9.1 - i4.5$
$43.8 - i33.8$	$57.1 - i26.5$	$47.8 - i38.3$	$50.2 - i23.2$
$55.5 - i23.9$	$73.6 - i26.3$	$51.2 - i22.0$	$62.1 - i46.4$
$9.0 + i4.6$	$9.1 + i4.6$	$33.3 + i22.6$	$43.0 + i57.5$
$43.8 + i33.8$	$57.1 + i26.5$	$42.5 + i57.3$	$48.5 + i33.2$
$55.5 + i23.9$	$73.6 + i26.3$	$62.3 + i19.4$	

Table 5: Poles of the two-channel  $S$ -matrix on all the principal sheets of the Riemann surface (see Fig. 3). The energy is counted from the  $dt$ -threshold.

For the coupled channels 1 and 2, we found three resonances on the non-physical Riemann sheet,  $(--)_0$ , with the parameters given in Table 4. As was expected from our qualitative reasoning, the partial widths for the  $dt$ -channel turned out to be significantly smaller than the corresponding widths for the  $n\alpha$ -channel. In the (uncoupled) channels 3 and 4, no resonances were found.

By scanning all four principal sheets of the Riemann surface within a distance of  $\sim 50$  keV around the central energy  $E_0$ , we found several  $S$ -matrix poles on each of the sheets. These poles are listed in Table 5.

The poles that are adjacent to the physical scattering energies and therefore may have influence on physical observables, are those given in the left bottom and right upper blocks of this Table. It is seen that the poles on the sheets  $(++)_0$  and  $(-+)_0$  have the “mirror” partners while this is not the case for the sheets  $(--)_0$  and  $(+-)_0$ . This is a consequence of the fact that the Coulomb interaction breaks down the “mirror” symmetry and in our problem

the Coulomb potential is only present in the second channel. A more detailed explanation can be found in the Appendix A.2.

There was a possibility that some of the poles might be spurious, i.e. appearing as a result of the truncation of the Taylor series (21) and (22). The reason for possible appearance of the spurious poles can be understood using the following simple example. Consider the exponential function  $e^z$  that does not have zeros anywhere on the complex  $z$ -plane. However, if it is approximated by a finite number of the Taylor terms, it becomes a polynomial that has  $N$  zeros, where  $N$  is its highest power. Apparently, all such zeros are spurious.

In our case, each  $S$ -matrix pole corresponds to a zero of the Jost matrix determinant (see Eqs. (7) and (8)), and the Jost matrix obtained by fitting the experimental data, involves the polynomials (21) and (22). Of course there are many other (non-polynomial) factors in the Jost matrices, but a possibility that some spurious zeros may appear cannot be excluded. In a more simple (non-Coulomb) problem the existence of such spurious zeros was demonstrated in Ref [32].

As with any spurious solutions, there is a simple recipe to identify them: they are unstable and drastically change as a result of any small changes in the parameters of the problem. In our problem, there is a parameter whose choice is rather arbitrary and the results should not depend on such a choice. This is the center  $E_0$  of the Taylor expansions (21) and (22). These expansions are valid within a circle around  $E_0$  and therefore it should be chosen somewhere not far from the energy where it is expected to find resonances. Of course for different choices of  $E_0$  the fitting parameters  $\mathbf{a}^{(m)}$  and  $\mathbf{b}^{(m)}$  are different, but the non-spurious zeros of the Jost matrix determinant must be the same.

In order to check if the poles listed in Table 5 are non-spurious, we repeated the fit with  $E_0 = 40$  keV and  $E_0 = 60$  keV (in addition to our original fit with  $E_0 = 50$  keV). The quality of these fits are the same as shown in Figs. 8, 9, 10, and 11. The corresponding parameters  $\mathbf{a}^{(m)}$  and  $\mathbf{b}^{(m)}$  are given in Table 2. As is seen, the fitting parameters are indeed very different for the three choices of  $E_0$ . However, the positions of all the poles listed in Table 5, turned out to be stable with respect to the variations of  $E_0$  (the changes are in the fourth digit). On these grounds, we conclude that all these poles are meaningful, i.e. non-spurious.

In Table 6, for the purpose of comparison, we list the poles reported in several other publications [4–7, 18]. As is seen, we found much more poles. However, it should be noted that we do not contradict the previous findings. Indeed, Our resonance at the energy  $\sim (50 - i23)$  keV on the sheet  $(--)_0$  is not far from the pole  $\sim (47 - i37)$  keV (on the same sheet) reported by the other authors (see Table 6). And one of our “shadow” poles, namely, at  $\sim (74 - i26)$  keV on the sheet  $(-+)_0$ , is not far from the corresponding “shadow” poles obtained in the other publications that are cited in Table 6. Of course, there are some differences, but they are not too big. We therefore can say that we have located the same poles but at somewhat shifted points.



resonances (keV)	shadow poles (keV)	sheet	Ref.	year
$48.10 - i37.08$	$78.94 - i8.26$	(??)	[4]	1987
$46.97 - i37.1$	$81.57 - i3.64$	(-+)	[5]	1987
$47 - i36$	$77 + i14$	(?-)	[6]	1990
$47 - i37$	$82 - i3.4$	(-+)	[7]	1991
$48 - i41$	$88 - i21$	(-+)	[18]	2018

Table 6: The resonant and the shadow  $S$ -matrix poles in the state  $\frac{3}{2}^+$  near the  $dt$ -threshold, reported in several publications. The question marks mean that the authors did not give the corresponding signatures (identities) of the Riemann sheets.

As to the other poles we found, there are several possible reasons why they were missed previously. It might be that nobody actually searched for poles in the locations that were considered as being “inappropriate”. In fact there is no rigorous mathematical theory that would tell us where the poles of a multi-channel  $S$ -matrix can be and where cannot. Yet another possible reason for the differences between the Tables 5 and 6 may be rooted in the different analytic structure of the functions used for the analytic continuation. As an example of such a difference it can be mentioned the following. In the  $R$ -matrix theory the  $S$ -matrix is a ratio of two matrices, both of which have poles on the real axis. Within our approach, the  $S$ -matrix is also a ratio of two (Jost) matrices, but they do not have poles at real energies.

In order to pinpoint the actual cause of the difference, it is needed to perform a mathematically rigorous analysis of the analytic structure of the  $R$ -matrix, of the  $S$ -matrix derived from it, and of the topology of the Riemann surface on which they are defined. To the best of our knowledge, nobody ever did such an analysis and many of the  $R$ -matrix properties on the Riemann surface are tacitly assumed.

Some erroneous assumptions might lead to wrong conclusions. For example, in Fig. 5 of Ref. [7] it is assumed that one can continuously move from the lower half of the sheet  $(-+)_0$  (denoted in [7] as  $U_{(2)}$ ) across the connected rims of the cut to the upper half of the sheet  $(+-)_0$  (denoted as  $U_{(1)}$ ). According to our analysis (see Fig. 3), this is wrong. It would be correct without the Coulomb interaction. But in the presence of the Coulomb forces the number of the Riemann sheets becomes infinite and some of their interconnections become different.

Moreover, as we show in the Appendix A, the Coulomb forces break down most of the symmetry relations among the elements of the  $S$ -matrix on different sheets of the Riemann

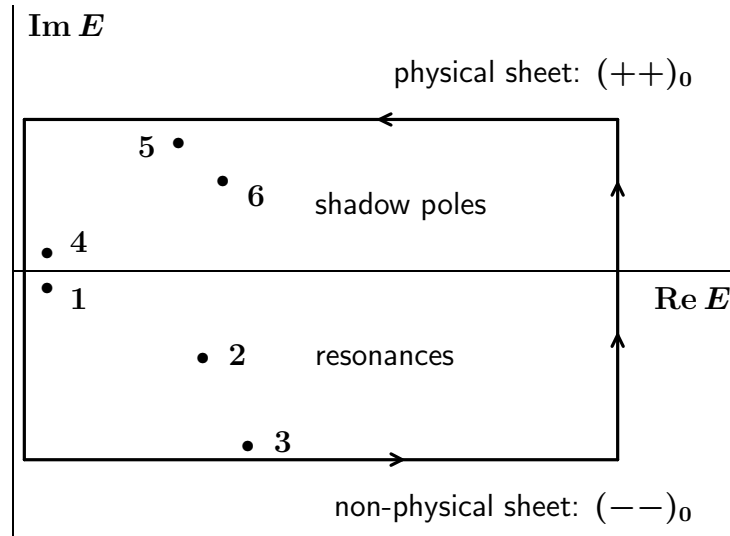


Figure 14: The  $S$ -matrix poles located around the real axis of the scattering energies that connects the physical and non-physical sheets of the Riemann surface. The complex values of the corresponding energies can be found in Tables 5 and 7. The numerical labels of the poles are used as the corresponding references in Fig. 15. The rectangular contour is used for the integration in the Mittag-Leffler sum (32).

surface. As a result, the reasoning about the role of the shadow poles, given by Eden and Taylor in Ref. [35], is not applicable for the charged particles. However, most of the authors base their conclusions on the so-called “generalized unitarity” of Ref. [35].

The elastic and inelastic scattering can only be affected by the poles that are close to the real axis where the physical and non-physical sheets  $(++)_0$  and  $(--)_0$  are connected. All the other poles are too far. Indeed, it is necessary to go around one or more branch points in order to reach the scattering energies from them.

Therefore among the 23 poles given in Table 5, there are six poles which may influence the collision process. As is shown in Fig. 14, they are on both sides of the real axis which is between  $(++)_0$  and  $(--)_0$ . The poles with negative imaginary parts are the usual resonances, and those above the real axis are the shadow poles.

In order to learn about the importance of each of these six poles for the scattering process, we apply the method used in Ref. [33]. This method is based on the Mittag-Leffler theorem (see, for example, Ref. [34]), which allows one to split a meromorphic function in the pole and the non-singular (background) terms. This is what is described next.

## 5.1 Contributions from individual poles

Let us consider the closed rectangular contour shown in Fig. 14, which goes around the poles nearest to the real scattering energies, i.e. the poles on the interconnected sheets  $(++)_0$  and  $(--)_0$  of the Riemann surface. If  $E$  is a point inside this contour (we choose it on the real axis), then according to the residue theorem, we have

$$\oint \frac{\mathbf{S}(\zeta)}{\zeta - E} d\zeta = 2\pi i \mathbf{S}(E) + 2\pi i \sum_{j=1}^L \frac{\text{Res}[\mathbf{S}, E_j]}{E_j - E}, \quad (31)$$

where  $E_j$  are the poles enclosed by the contour ( $L = 6$ ). Therefore

$$\mathbf{S}(E) = \sum_{j=1}^L \frac{\text{Res}[\mathbf{S}, E_j]}{E - E_j} + \frac{1}{2\pi i} \oint \frac{\mathbf{S}(\zeta)}{\zeta - E} d\zeta, \quad (32)$$

which is a particular formulation of the more general Mittag-Leffler theorem. In Eq. (32) the  $S$ -matrix  $\mathbf{S}(E)$  on the real axis is written as a sum of the contributions from each pole and a background integral.

After fitting the experimental data, we obtain the analytic formulae for the Jost matrices and hence for the  $S$ -matrix. This allows us to (numerically) calculate the background integral for any given scattering energy  $E$ . The poles  $E_j$  are known. We assume that all the poles are simple. Therefore the residues at them can be found by numerical differentiation of the determinant of the Jost matrix. Indeed,

$$\mathbf{S} = \mathbf{f}^{(\text{out})} \begin{pmatrix} f_{22}^{(\text{in})} & -f_{12}^{(\text{in})} \\ -f_{21}^{(\text{in})} & f_{11}^{(\text{in})} \end{pmatrix} \frac{1}{\det \mathbf{f}^{(\text{in})}} \quad (33)$$

and thus

$$\text{Res}[\mathbf{S}, E] = \mathbf{f}^{(\text{out})}(E) \begin{pmatrix} f_{22}^{(\text{in})}(E) & -f_{12}^{(\text{in})}(E) \\ -f_{21}^{(\text{in})}(E) & f_{11}^{(\text{in})}(E) \end{pmatrix} \left[ \frac{d}{dE} \det \mathbf{f}^{(\text{in})}(E) \right]^{-1}, \quad (34)$$

where

$$\frac{d}{dE} \det \mathbf{f}^{(\text{in})}(E) \approx \frac{\det \mathbf{f}^{(\text{in})}(E + \epsilon) - \det \mathbf{f}^{(\text{in})}(E - \epsilon)}{2\epsilon}. \quad (35)$$

In our calculations, we used  $\epsilon = 1 \text{ eV}$  which gave the accuracy of at least 5 digits. Thus calculated residues for the six poles are given in Table 7. With these residues and with the

sheet	pole: $E$ (keV)	$\text{Res}[S_{nn'}, E]$ (keV)	$n, n'$
$(--)_0$	$9.1 - i4.5$	$0.023681 - i0.036357$	1,1
		$0.0035344 - i0.0036706$	1,2
		$0.47319 + i0.087305$	2,1
		$0.052651 + i0.020520$	2,2
	$50.2 - i23.2$	$-0.51181 + i0.65675$	1,1
		$-0.28605 + i0.28668$	1,2
		$-9.2422 + i5.9593$	2,1
		$-4.8154 + i2.3285$	2,2
	$62.1 - i46.4$	$1.7887 - i14.855$	1,1
		$2.2774 + i1.5480$	1,2
		$36.478 + i49.327$	2,1
		$-11.147 + i1.7942$	2,2
$(++)_0$	$9.0 + i4.6$	$-0.024456 + i0.039395$	1,1
		$-0.0073593 + i0.0027477$	1,2
		$-0.092407 + i0.73479$	2,1
		$-0.088505 + i0.088928$	2,2
	$43.8 + i33.8$	$-12.589 + i14.992$	1,1
		$1.7237 - i0.63052$	1,2
		$39.860 - i30.546$	2,1
		$-4.6670 + i0.62084$	2,2
	$55.5 + i23.9$	$1.1959 + i2.0737$	1,1
		$0.56551 + i0.17848$	1,2
		$14.951 + i1.5362$	2,1
		$2.9874 - i2.2224$	2,2

Table 7: Poles of the two-channel  $S$ -matrix and the corresponding residues of its elements in the domains of the Riemann sheets  $(--)_0$  and  $(++)_0$  adjacent to the axis of the real scattering energies (see Fig. 3). The energy is counted from the  $dt$ -threshold.

numerically calculated background integral (the contour was extended up to 200 keV and on each line-segment of the contour it were used 400 Gauss-Legendre integration points) we obtained (as it should be) exactly the same cross sections that are shown in Figs. 8, 9, 10, and 11. This is a kind of cross-check of our calculations. Moreover this fact is an additional proof that there is no other poles (apart from the six poles shown in Fig. 14) inside the contour.

Now we can omit some of the poles from the sum (32) and see how this affects the partial cross sections. The results of such an analysis (where we excluded only one pole at a time) are shown in Fig. 15. The curves show the cross sections when one pole is excluded. The dots are the experimental data (i.e. the  $R$ -matrix cross sections).

It is seen that the first resonance as well as the first shadow pole (poles 1 and 4, respectively) practically do not affect the cross sections at all (their effect is in the fourth digit). This means that these two poles can be safely ignored. The exclusion of the second resonance (pole number 2) makes noticeable changes only in the elastic  $dt \rightarrow dt$  scattering. Meanwhile, the third resonance (pole number 3) is important for all four (elastic and inelastic) processes. Among the three shadow poles, the second one (pole number 5) is the most important. Its contribution to all four processes is comparable with the effect of the second resonance. The third shadow pole (pole number 6) makes just “cosmetic” changes to all the partial cross sections.

It is also interesting to know what happens if we exclude all the pole terms from the Mittag-Leffler expansion (32) and only leave the background integral. Fig. 16 shows the result of such an exclusion. As is seen, without the resonant and the shadow poles all the cross sections are far from the experimental points. In the channels  $2 \rightarrow 1$  and  $2 \rightarrow 2$  the background integral is responsible for the sharp peaks near the threshold energy.

## 6 Summary and conclusion

As was stated in the Introduction, the main question that we wanted to answer in the present work was about the nature of  ${}^5\text{He}^*(\frac{3}{2}^+)$ -resonance. Using an available  $R$ -matrix fit as our input (experimental) data, we constructed the corresponding Jost-matrices that have proper analytic structure and are defined on the Riemann surface with the proper topology (where both the square-root and logarithmic branching are present). Exploring their behaviour on various sheets of the Riemann surface, we located 23 poles of the  $S$ -matrix. Only 6 of these poles turned out to be close enough to the axis of the real scattering energies and therefore only these 6 poles could influence the observable quantities. The set of these 6 poles consists of 3 resonances and 3 shadow poles.

Using the Mittag-Leffler representation, we isolated the individual contributions to the  $S$ -matrix from all the resonances and the shadow poles. In this way it was established that the

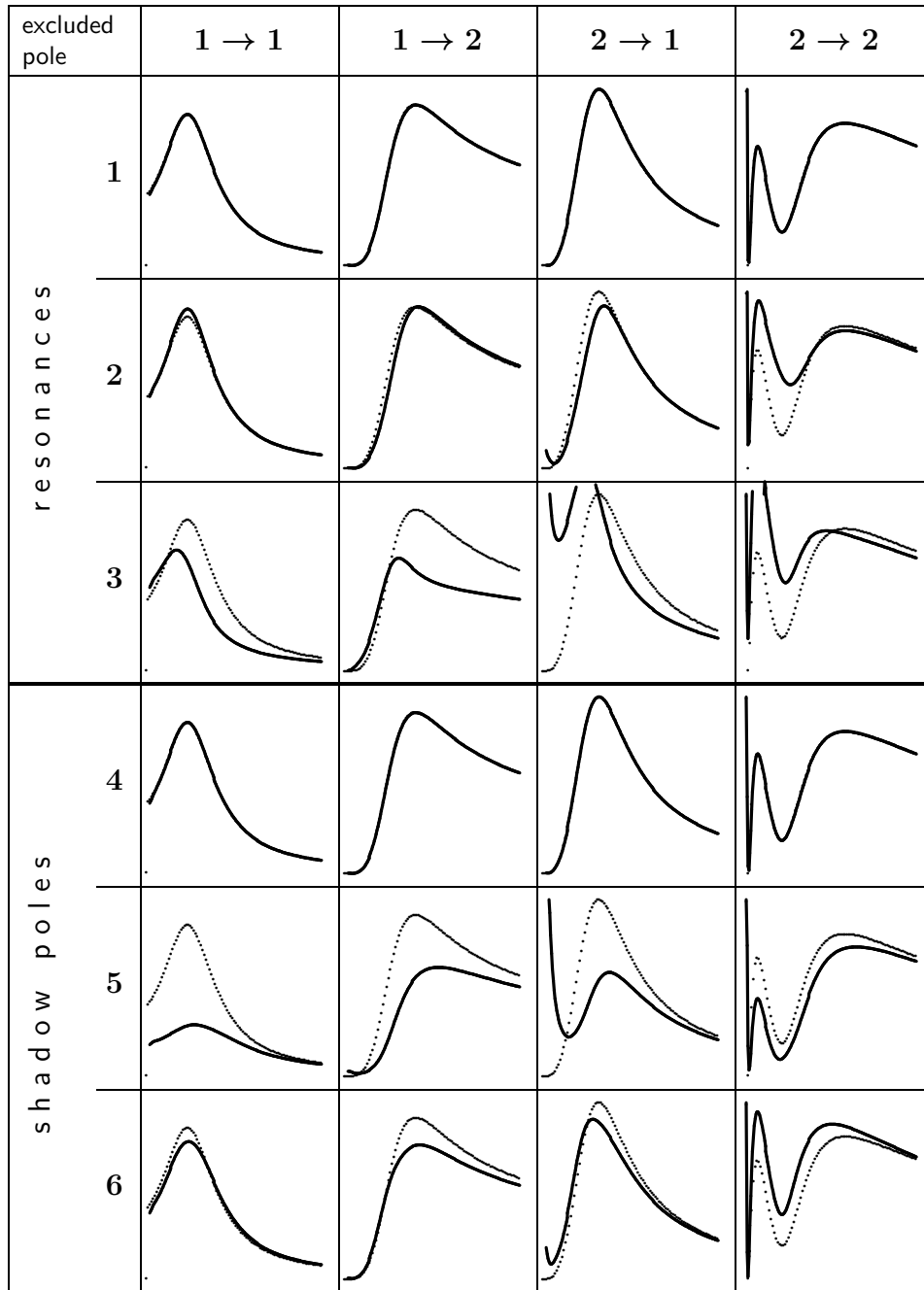


Figure 15: Partial cross sections (the curves) for the inter-channel transitions  $n \rightarrow n'$ , when a single pole is excluded from the Mittag-Leffler sum (32). The channels are labeled as in Table 1. The poles are numbered as is shown in Fig. 14. The dots are the corresponding experimental (i.e. the  $R$ -matrix) cross sections.

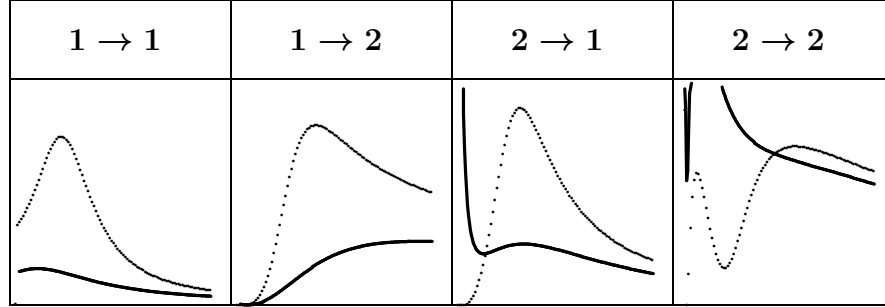


Figure 16: Partial cross sections for the inter-channel transitions  $n \rightarrow n'$ , when all six poles shown in Fig. 14 are excluded from the Mittag-Leffler sum (32). The dots are the corresponding experimental (i.e. the  $R$ -matrix) cross sections.

energy dependencies of the partial cross sections near the  $dt$ -threshold are mainly determined by the two resonant poles,

$$\begin{aligned} & \left( 50.2 - \frac{i}{2}46.3 \right) \text{ keV} , \quad \Gamma_{n\alpha} = 29.1 \text{ keV} , \quad \Gamma_{dt} = 17.2 \text{ keV} , \\ & \left( 62.1 - \frac{i}{2}92.8 \right) \text{ keV} , \quad \Gamma_{n\alpha} = 76.6 \text{ keV} , \quad \Gamma_{dt} = 16.2 \text{ keV} , \end{aligned}$$

and two shadow poles at  $(43.8 + i33.8) \text{ keV}$  and  $(55.5 + i23.9) \text{ keV}$  on the principal physical sheet  $(++)_0$ . The contribution of the other pair of the resonance and its shadow (at around  $\sim 9 \text{ keV}$ ) is negligible and can be ignored. The non-resonant background scattering is responsible for the threshold cusps in the channels  $dt \rightarrow n\alpha$  and  $dt \rightarrow dt$ .

## Appendices

### A Symmetry properties of the Jost matrices

The matrices  $f^{(\text{in})}$  and  $f^{(\text{out})}$  are related to each other at different points of the Riemann surface, i.e. they obey certain symmetry rules. Since the unknown matrices  $\mathbf{A}$  and  $\mathbf{B}$  in the semi-analytic representations (17) and (20) are the same on all the sheets, the symmetry relations among the Jost matrices are determined by the explicitly given factors that undergo certain changes when we replace  $k_n$  with  $-k_n$  or with  $k_n^*$ . For the sake of clarity, we firstly consider the simplified representation (20) for neutral particles. Then, using the more general

Eq. (17), we show that the Coulomb forces break some of the symmetries.

## A.1 Neutral particles

The energy variable  $E$  determines all the channel momenta, but not completely. There is the freedom to choose their signs. Different signs of them place the corresponding point on this or that sheet of the Riemann surface. In order to specify which sheet of the surface the point belongs to, it is convenient to replace the notation  $\mathbf{f}^{(\text{in/out})}(E)$  with  $\mathbf{f}^{(\text{in/out})}(k_1, k_2, \dots, k_N)$ . To simplify the formulae, we will write them for  $N = 2$ .

Replacing  $(k_1, k_2)$  with  $(-k_1, -k_2)$  in Eq. (20), we see that the factorized momenta generate a common factor  $(-1)^{\ell_m + \ell_n} = (-1)^{\ell_m - \ell_n}$  and the sign between the two terms, i.e the  $(\mp)$ , is changed to the opposite,  $(\pm)$ . This means that

$$f_{mn}^{(\text{in/out})}(-k_1, -k_2) = (-1)^{\ell_m + \ell_n} f_{mn}^{(\text{out/in})}(k_1, k_2) . \quad (36)$$

The change  $(k_1, k_2) \rightarrow (-k_1, -k_2)$  is equivalent to moving to a different sheet of the Riemann surface, namely,  $(++) \leftrightarrow (--)$  or  $(-+) \leftrightarrow (+-)$ . Such a transition is done to a point that is above or below the initial location on a vertical line that corresponds to the same energy. If the parity is conserving, then  $(-1)^{\ell_m + \ell_n} = 1$  and Eq. (36) relates the whole matrices,

$$\mathbf{f}^{(\text{in/out})}(-k_1, -k_2) = \mathbf{f}^{(\text{out/in})}(k_1, k_2) . \quad (37)$$

This can be called the ‘‘vertical’’ symmetry. It is schematically shown in Fig. 17, where

$$\begin{aligned} \mathbf{f}^{(\text{in/out})}(1) &= \mathbf{f}^{(\text{out/in})}(7) , & \mathbf{f}^{(\text{in/out})}(3) &= \mathbf{f}^{(\text{out/in})}(5) , \\ \mathbf{f}^{(\text{in/out})}(2) &= \mathbf{f}^{(\text{out/in})}(8) , & \mathbf{f}^{(\text{in/out})}(4) &= \mathbf{f}^{(\text{out/in})}(6) . \end{aligned}$$

One more symmetry property can be derived using the Schwartz reflection principle, which reads (see, for example Ref. [25]): If a function  $f(z)$  is analytic in a domain  $D$  that includes a line segment  $L$ , and  $f(z)$  is real on  $L$ , then this function can be analytically continued across  $L$  into the domain  $\overline{D}$ , which is a mirror reflection of  $D$  relative to the line  $L$ , and the values of  $f(z)$  at any two points symmetric with respect to  $L$  are complex conjugates of each other. It is graphically illustrated in Fig. 18.

The functions (matrices)  $\mathbf{A}(E)$  and  $\mathbf{B}(E)$  are real on the real axis [19, 20]. Therefore

$$\mathbf{A}(E^*) = \mathbf{A}^*(E) , \quad \mathbf{B}(E^*) = \mathbf{B}^*(E) . \quad (38)$$

The change  $E \rightarrow E^*$  is equivalent to  $(k_1, k_2) \rightarrow (k_1^*, k_2^*)$ , which implies that

$$f_{mn}^{(\text{in/out})}(E^*) = \left( \frac{k_n^{\ell_n + 1}}{k_m^{\ell_m + 1}} \right)^* A_{mn}(E^*) - i (k_m^{\ell_m} k_n^{\ell_n + 1})^* B_{mn}(E^*) = [f_{mn}^{(\text{out/in})}(E)]^* ,$$



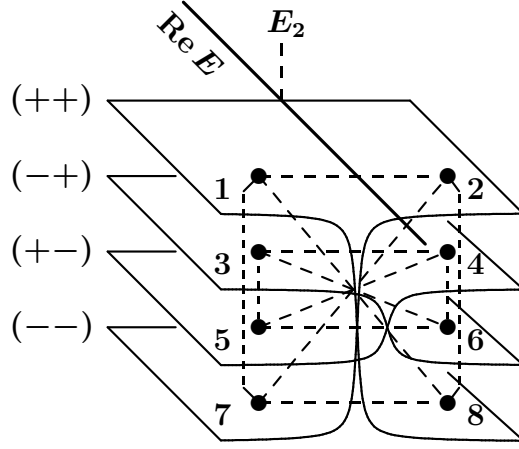


Figure 17: Fragment of the Riemann surface for a two-channel problem of neutral particles. The interconnections of the sheets are shown for the energies above the second threshold,  $E_2$ . The points with the odd numbers correspond to the same energy  $E$ , while the points with the even numbers correspond to the complex conjugate energy  $E^*$ . The dashed lines connect the points at which the values of the Jost matrices are related according to Eqs. (37), (39), and (42).

and thus

$$\mathbf{f}^{(\text{in/out})}(E^*) = [\mathbf{f}^{(\text{out/in})}(E)]^* . \quad (39)$$

Apparently, when replacing the energy variable  $E$  with its complex conjugate partner,  $E^*$ , the imaginary parts of all the channel momenta change their signs. As a result, the point  $E^*$  is on the other side of the real axis and on a different sheet of the Riemann surface, which can symbolically be written as follows:

$$E \rightarrow E^* \quad \Rightarrow \quad (\text{sign}_1, \text{sign}_2) \rightarrow (-\text{sign}_1, -\text{sign}_2) . \quad (40)$$

The symmetry (39) is valid for each pair of the sheets having the opposite signatures as in Eq. (40), and can be called the “diagonal” symmetry. It is schematically shown by the diagonal dashed lines in Fig. 17, where

$$\begin{aligned} \mathbf{f}^{(\text{in/out})}(1) &= \mathbf{f}^{(\text{out/in})^*}(8) , & \mathbf{f}^{(\text{in/out})}(3) &= \mathbf{f}^{(\text{out/in})^*}(6) , \\ \mathbf{f}^{(\text{in/out})}(5) &= \mathbf{f}^{(\text{out/in})^*}(4) , & \mathbf{f}^{(\text{in/out})}(7) &= \mathbf{f}^{(\text{out/in})^*}(2) . \end{aligned} \quad (41)$$

We can combine the “vertical” and “diagonal” symmetries stated by Eqs. (37) and (39), which gives

$$\mathbf{f}^{(\text{in/out})}(k_1, k_2) = [\mathbf{f}^{(\text{in/out})}(-k_1^*, -k_2^*)]^* . \quad (42)$$

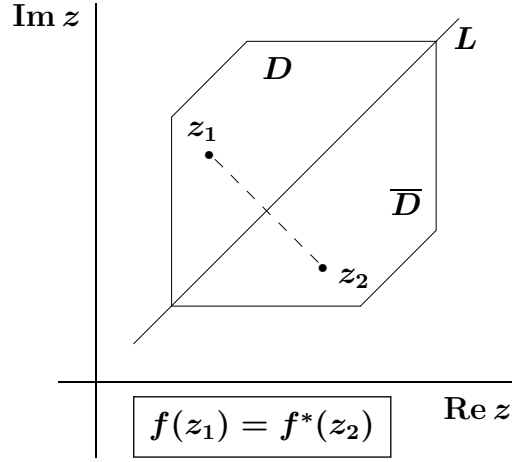


Figure 18: Illustration of the Schwartz reflection principle.

When changing the sign,  $k_n \rightarrow -k_n$ , we change the sign of  $\text{Im } k_n$ . And the complex conjugation brings the same sign back. Therefore the two points  $(k_1, k_2)$  and  $(-k_1^*, -k_2^*)$  are on the same Riemann sheet, but on the opposite sides of the cut. As a result, we obtain the symmetry relation along the horizontal lines shown in Fig. 17, where

$$\begin{aligned} \mathbf{f}^{(\text{in/out})}(1) &= \mathbf{f}^{(\text{in/out})^*}(2) , & \mathbf{f}^{(\text{in/out})}(3) &= \mathbf{f}^{(\text{in/out})^*}(4) , \\ \mathbf{f}^{(\text{in/out})}(5) &= \mathbf{f}^{(\text{in/out})^*}(6) , & \mathbf{f}^{(\text{in/out})}(7) &= \mathbf{f}^{(\text{in/out})^*}(8) . \end{aligned}$$

This is known as the “mirror symmetry”. Apparently, if there is a spectral points at the energy  $E$ , for example, if  $\det \mathbf{f}^{(\text{in})}(7) = 0$ , then there is a “mirror” resonance at the point 8 (see Fig. 17). In the two-channel case, the “mirror” resonances can be between the thresholds  $E_1$  and  $E_2$  on the sheet  $(-+)$  on the other side of the cut, and for possible resonances above the threshold  $E_2$  they are on the sheet  $(--)$  also on the opposite side of the cut. In order to reach the real axis of the physical sheet  $(++)$  from such “mirror” resonances, we have to go around one and two branch points, respectively. This means that they are far away from the scattering energies and thus their influence on the observable quantities is very weak, if any.

Using the definition (8) and the symmetries of the Jost matrices shown in Fig. 17, it is easy to derive the corresponding symmetry-relations for the  $S$ -matrix. For example,

$$\begin{aligned} \mathbf{S}(1) &= [\mathbf{S}^{-1}(8)]^* , & \mathbf{S}(3) &= [\mathbf{S}^{-1}(6)]^* , \\ \mathbf{S}(5) &= [\mathbf{S}^{-1}(4)]^* , & \mathbf{S}(7) &= [\mathbf{S}^{-1}(2)]^* . \end{aligned}$$

It should not be forgotten that this is only valid when  $(-1)^{\ell_m + \ell_n} = 1$ , i.e. for the potentials that conserve the parity.

## A.2 Interaction involving a Coulomb tail

If the multi-channel potential has a Coulomb tail at least in one of the channels, some of the symmetries symbolically depicted in Fig. 17, are broken. This can be shown by analysing the analytic structure given by Eq. (17), which we can re-write in the matrix form as follows,

$$\mathbf{f}^{(\text{in/out})} = \mathbf{Q}^{(\pm)} [\mathbf{D}^{-1} \mathbf{A} \mathbf{D} - (\mathbf{M} \pm i) \mathbf{K}^{-1} \mathbf{D} \mathbf{B} \mathbf{D}] , \quad (43)$$

where the (depending on the energy) diagonal matrices  $\mathbf{Q}^{(\pm)}(E)$ ,  $\mathbf{D}(E)$ ,  $\mathbf{M}(E)$ , and  $\mathbf{K}(E)$  are defined as (see Ref. [20]):

$$\mathbf{Q}^{(\pm)} = \text{diag} \left\{ \frac{e^{\pi\eta_1/2} \ell_1!}{\Gamma(\ell_1 + 1 \pm i\eta_1)}, \frac{e^{\pi\eta_2/2} \ell_2!}{\Gamma(\ell_2 + 1 \pm i\eta_2)}, \dots, \frac{e^{\pi\eta_N/2} \ell_N!}{\Gamma(\ell_N + 1 \pm i\eta_N)} \right\} , \quad (44)$$

$$\mathbf{D} = \text{diag} \left\{ C_{\ell_1}(\eta_1) k_1^{\ell_1+1}, C_{\ell_2}(\eta_2) k_2^{\ell_2+1}, \dots, C_{\ell_N}(\eta_N) k_N^{\ell_N+1} \right\} , \quad (45)$$

$$\mathbf{M} = \text{diag} \left\{ \frac{2\eta_1 h(\eta_1)}{C_0^2(\eta_1)}, \frac{2\eta_2 h(\eta_2)}{C_0^2(\eta_2)}, \dots, \frac{2\eta_N h(\eta_N)}{C_0^2(\eta_N)} \right\} , \quad (46)$$

$$\mathbf{K} = \text{diag} \{k_1, k_2, \dots, k_N\} . \quad (47)$$

First of all, let us consider what happens if we change the sign of a channel momentum  $k_n$ . The sign can be changed by the exponential factor

$$k_n \rightarrow -k_n : \quad e^{i\pi(2j+1)k_n} , \quad j = \pm 1, \pm 2, \dots \quad (48)$$

For the channel  $n$  without a Coulomb potential, all values of  $j$  in such a factor are equivalent. However, if there are Coulomb forces in the channel  $n$ , then the functions involved in the matrices of Eq. (43), undergo the following changes:

$$k_n \rightarrow e^{i\pi(2j+1)k_n} \Rightarrow \begin{cases} \eta_n \rightarrow -\eta_n , \\ C_{\ell_n}(\eta_n) \rightarrow e^{\pi\eta_n} C_{\ell_n}(\eta_n) , \\ h(\eta_n) \rightarrow h(\eta_n) + i\pi(2j+1) . \end{cases} \quad (49)$$

Apparently, after the change of the sign of a channel momentum, these functions have different values and thus the relation (36), generally speaking, cannot be valid anymore. In other words, the ‘‘vertical’’ symmetry is broken by the Coulomb forces.

It is easy to see that the “diagonal” symmetry that follows from the Schwartz reflection principle, remains valid in the presence of the Coulomb potential. The “diagonal” transition  $E \rightarrow E^*$  moves the point to the other side of the real axis. Both the original point  $E$  and the new point  $E^*$  can be on any of the Riemann sheets. It is clear that the complex conjugation of the energy results in the complex conjugation of all the channel momenta and thus of all the Sommerfeld parameters,

$$E \rightarrow E^* \Rightarrow k_n \rightarrow k_n^*, \quad \eta_n \rightarrow \eta_n^*, \quad \forall n .$$

The transition  $k_n \rightarrow k_n^*$  changes the sign of  $\text{Im } k_n$ . This means that the point  $E^*$  is on a different sheet of the Riemann surface. Actually, all the signs in the sheet-label  $(\pm, \pm, \dots)_{m_1 m_2, \dots}$  are changing to the opposite, as is given by Eq. (40). Apparently, the logarithmic indices,  $m_1 m_2, \dots$ , change to the opposite as well. This can be seen from Eq. (13) that defines them.

It is clear that  $\mathbf{Q}^{(\pm)}(E^*) = [\mathbf{Q}^{(\mp)}(E)]^*$ ,  $\mathbf{D}(E^*) = [\mathbf{D}(E)]^*$ ,  $\mathbf{M}(E^*) = [\mathbf{M}(E)]^*$ , and  $\mathbf{K}(E^*) = [\mathbf{K}(E)]^*$ . Taking into account the Schwartz relations (38), we therefore arrive at the same symmetry property (39),

$$\mathbf{f}^{(\text{in/out})}(E_{m_1 m_2, \dots}^*) = [\mathbf{f}^{(\text{out/in})}(E_{-m_1, -m_2, \dots})]^* , \quad (50)$$

where the subscripts (logarithmic indices  $m_1, m_2, \dots$ ) of the energy variable specify the sheet of the Riemann surface. The corresponding relations for the  $S$ -matrix can be obtained as follows:

$$\begin{aligned} \mathbf{S}(E_{m_1 m_2, \dots}^*) &= \mathbf{f}^{(\text{out})}(E_{m_1 m_2, \dots}^*) [\mathbf{f}^{(\text{in})}(E_{m_1 m_2, \dots}^*)]^{-1} \\ &= \mathbf{f}^{(\text{in})*}(E_{-m_1, -m_2, \dots}) [\mathbf{f}^{(\text{out})*}(E_{-m_1, -m_2, \dots})]^{-1} \\ &= \left\{ \mathbf{f}^{(\text{out})*}(E_{-m_1, -m_2, \dots}) [\mathbf{f}^{(\text{in})*}(E_{-m_1, -m_2, \dots})]^{-1} \right\}^{-1} \\ &= [\mathbf{S}^*(E_{-m_1, -m_2, \dots})]^{-1} . \end{aligned} \quad (51)$$

It should not be forgotten that the transition  $E_{m_1 m_2, \dots}^* \rightarrow E_{-m_1, -m_2, \dots}$  moves the point to a different sheet of the Riemann surface, where all the labels are changing to the opposite, for example,

$$(++)_{1,0,-1} \rightarrow (--)_{-1,0,1} .$$

In particular, the relation (51) means that a resonance pole of the  $S$  matrix corresponds to a zero of its determinant at the symmetric point on the physical sheet of the Riemann surface.

For a two-channel problem, the diagonal relations (50) are illustrated in Fig. 19. Of course there are much more (actually infinite number of) “diagonal” relations of the type (50). Fig. 19

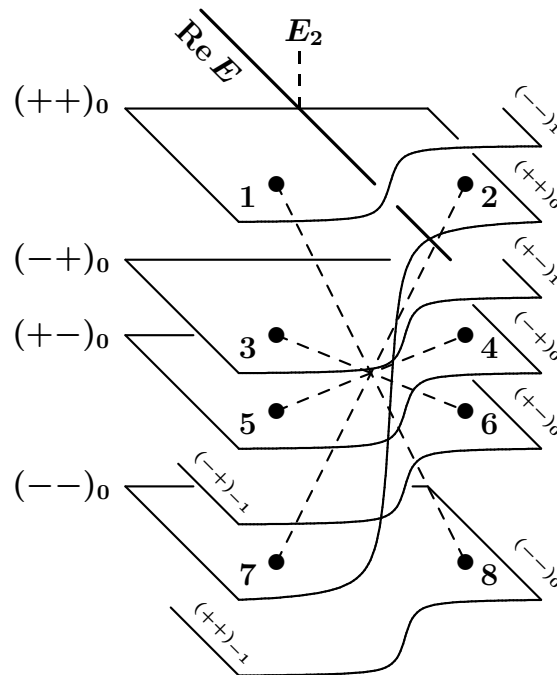


Figure 19: Fragment of the Riemann surface shown in Fig. 3(b). The points with the odd numbers correspond to the same energy  $E$ , while the points with the even numbers correspond to the complex conjugate energy  $E^*$ . The four dashed lines connect the points at which the values of the Jost matrices are related according to Eq. (50).

only shows the symmetric points on the principal branch of the Riemann surface. The other sheets (with non-zero logarithmic indices) have no practical influence on the observables and thus can be safely ignored. In this figure, the points labeled by the odd numbers, are on the same vertical line and thus correspond to the same energy  $E$ . The even numbers label the symmetric complex conjugate energies,  $E^*$ . The diagonal dashed lines correspond to the four relations given by Eq. (41). It is instructive to compare the relations depicted in Fig. 19 with the corresponding relations for the neutral particles given in Fig. 17.

Since there are no “vertical” symmetries for the charged particles, the “horizontal” symmetries (that result from the combination of the “diagonal” and “vertical” ones) are also broken. In particular, this means that there are no “mirror” poles of the  $S$ -matrix, if the charges are non-zero. For example, if the point 7 in Fig. 19 is a resonance, then the point 8 could be its “mirror” partner, but in contrast to the neutral-particle case (see Fig. 17), the points 7 and 8 are not related by a “horizontal” symmetry.

When doing the numerical calculations, we compared the Jost matrices at all the symmetric points shown in Fig. 19. In such a comparison, we observed the “diagonal” symmetry and did not see any other relations among the values of the Jost matrices. This is in accordance with the above analysis. However, we also (numerically) found an inexplicable relation, namely, the zeros of  $\det \mathbf{f}^{(\text{in})}$  at the energies  $E$  on the sheets  $(++)_0$  and  $(-+)_0$  have the “mirror” zeros at the corresponding points  $E^*$  on the same sheets, as if it were the “horizontal” symmetry for these sheets. The calculations at the nearby points show that there is no such a “horizontal” symmetry, but the zeros are still symmetric. It looks like the determinant is factorized in a symmetric and non-symmetric functions, but we could not proof this analytically.

## References

- [1] D.R. Tilley et al., “*Energy Levels of Light Nuclei  $A = 5, 6, 7$* ”, Nucl. Phys., **A708**, pp. 3-163(2002)
- [2] B.Haesner, W. Heeringa, H.O. Klages, H. Dobiach, G. Schmalz, P. Schwarz, J. Wilczynski, and B.Zeitnitz, “*Measurement of the  $^3\text{He}$  and  $^4\text{He}$  total neutron cross sections up to 40 MeV*”, Phys.Rev., **C28 (3)**, 995-999 (1983)
- [3] N. Jarmie, R. E. Brown, and R.A. Hardekopf, “*Fusion-energy reaction  $^2\text{H}(t, \alpha)n$  from  $E_t = 12.5$  to 117 keV*”, Phys.Rev., **C29 (6)**, 2031-2046 (1984); Erratum: Phys.Rev., **C33 (1)**, 385 (1986)
- [4] R.E. Brown, N. Jarmie, G.M. Hale “*Fusion-energy reaction  $^3\text{H}(d, \alpha)n$  at low energies*”, Phys.Rev., **C35 (6)**, 1999-2004 (1987)

- [5] G.M. Hale, Ronald E. Brown, Nelson Jarmie, “*Pole Structure of the  $J^\pi = \frac{3}{2}^+$  Resonance in  ${}^5\text{He}$* ”, Phys.Rev.Lett., **59**, 763-766 (1987)
- [6] B.M. Karnakov, V.D. Mur, S.G. Pozdnyakov, V.S. Popov, “*Analytic structure of the amplitude of  $dt$  scattering near the elastic threshold*”, JETP Lett., **51 (7)**, 399-402 (1990)
- [7] I.N. Bogdanova, G.M. Hale, V.E. Markushin, “*Analytical structure of the  $S$  matrix for the coupled channel problem  $d + t \rightarrow n + \alpha$  and the interpretation of the  $J^\pi = \frac{3}{2}^+$  resonance in  ${}^5\text{He}$* ”, Phys.Rev., **C44 (4)**, 1289-1295 (1991)
- [8] A. Csoto, R.G. Lovas, and A.T. Kruppa, “*Two-pole structure of the  $3/2^+$  resonance of  ${}^5\text{He}$  in a dynamical microscopical model*”, Phys. Rev. Lett. **70**, 1389 (1993)
- [9] V.D. Efros and H. Oberhummer, “*Ground-state energies and widths of the  ${}^5\text{He}$  and  ${}^5\text{Li}$  nuclei*”, Phys. Rev. **C54**, 1485 (1996)
- [10] A. Csoto and G.M. Hale, “*S-matrix and R-matrix determination of the low-energy  ${}^5\text{He}$  and  ${}^5\text{Li}$  resonance parameters*”, Phys. Rev. **C55**, 536 (1997)
- [11] F.C. Barker, “ *$\frac{3}{2}^+$  levels of  ${}^5\text{He}$  and  ${}^5\text{Li}$ , and shadow poles*”, Phys.Rev., **C56 (5)**, 2646-2653 (1997)
- [12] M. Drog, R. A. Ortiz, and B. Hoop, “*Re-evaluation of neutron- ${}^4\text{He}$  elastic scattering data near 20 MeV*”, Phys.Rev., **C83 (6)**, 064616 (2011)
- [13] B. Hoop, G.M. Hale, P. Navratil, “*Neutron- ${}^4\text{He}$  Resonant Scattering at  $d$ - ${}^3\text{H}$  Threshold*”, arXiv:nucl-th,1111.0985 (2012)
- [14] P. Navratil and S. Quaglioni, “*Ab initio many-body calculations of the  ${}^3\text{H}(d,n){}^4\text{He}$  and  ${}^3\text{He}(d,p){}^4\text{He}$  fusion reaction*”, Phys. Rev. Lett. **108**, 042503 (2012)
- [15] L.S. Brown and G.M. Hale, “*Field theory of the  $d + t \rightarrow n + \alpha$  reaction dominated by a  ${}^5\text{He}^*$  unstable particle*”, Phys. Rev. **C89**, 014622 (2014)
- [16] G.M. Hale, L.S. Brown, and M. W. Paris, “*Effective field theory as a limit of R-matrix theory for light nuclear reactions*”, Phys. Rev. **C89**, 014623 (2014)
- [17] B. Hoop, “*Interaction of neutrons with alpha particles: A tribute to Heinz Barschall*”, arXiv:1503.04855 [physics.hist-ph] (2015)

- [18] R.M. Id Betan, A.T. Kruppa, T. Vertse, “*Shadow poles in coupled-channel problems calculated with the Berggren basis*”, *Phys.Rev.*, **C97**, 024307 (2018)
- [19] S.A. Rakityansky, N. Elander, “*Multi-channel analog of the effective-range expansion*”, *J. Phys. A: Math. Theor.*, **44**, 115303 (2011)
- [20] S.A. Rakityansky, N. Elander, “*Analytic structure of the multichannel Jost matrix for potentials with Coulombic tails*”, *Journal of Mathematical Physics*, **54**, 122112 (2013)
- [21] S.A. Rakityansky, N. Elander, “*Analyzing the contribution of individual resonance poles of the S-matrix to two-channel scattering*”, *Int.J.Quant.Chem.*, **106**, 1105-1129, (2006)
- [22] K.F. Riley, M.P. Hobson, S.J. Bence, “*Mathematical Methods for Physics and Engineering*”, Chapter 16, Cambridge University Press (2008)
- [23] P. Fröbrich, R. Lipperheide, “*Theory of Nuclear reactions*”, Clarendon Press, Oxford (1996)
- [24] J.R. Taylor, “*Scattering Theory*”, Dover Publications, Inc., New York (2006)
- [25] R.P. Boas, “*Invitation to complex analysis*”, Random House, New York, 1987.
- [26] W.H. Press, S.A. Teukolsky, W.T. Vetterling, “*Numerical Recipes in Fortran 77*”, 2nd ed., Cambridge University Press (1997)
- [27] L.N. Bogdanova, V.E. Markushin, V.S. Melezhik, “*Nuclear widths and shifts of the dtμ mesic-molecule levels*”, *Sov. Phys. JETP*, **54(3)**, 442-448 (1981)
- [28] S.A. Rakityansky, N. Elander, “*A method for extracting the resonance parameters from experimental cross-sections*”, *International Journal of Modern Physics E*, Vol. 22, No. 5, 1350032 (17 pages), (2013)
- [29] P. Vaandrager, S.A. Rakityansky, “*Extracting the resonance parameters from experimental data on scattering of charged particles*”, *International Journal of Modern Physics E*, Vol. 25, No. 2, 1650014 (12 pages), (2016)
- [30] F. James and M. Roos, “*Minuit - a system for function minimization and analysis of the parameter errors and correlations*”, *Comp. Phys. Comm.* **10** (1975) 343-367; <http://hep.fi.infn.it/minuit.pdf>
- [31] S.A. Rakityansky, “*Partial widths of a multi-channel resonance*”, *Journal of Physics: Conf. Series*, Vol.915, 012008 (2017)



- [32] S.A. Rakityansky, N. Elander, “*Generalized effective-range expansion*”, *Journal of Mathematical Physics*, **42**, 225302 (2009)
- [33] S.A. Rakityansky, N. Elander, “*Analyzing the contribution of individual resonance poles of the S-matrix to two-channel scattering*”, *Int. J. Quantum Chem.*, **106**, 110529 (2006)
- [34] H. Jeffreys, B.S. Jeffreys, “*Methods of Mathematical Physics*”, p.383, 3rd Ed., Cambridge University Press, Cambridge, England (1988)
- [35] R.J. Eden, J.R. Taylor, “*Poles and shadow poles in the many-channel S matrix*”, *Phys.Rev.*, **133** (6), B1575-B1580 (1964)